Ain Shams Engineering Journal 16 (2025) 103460

Contents lists available at ScienceDirect

Ain Shams Engineering Journal

journal homepage: https://www.sciencedirect.com

Full Length Article

Artificial intelligence neural networking for data clustering of carbon dioxide model

Hasib Khan [a,b], Mahmoud Abdel-Aty [c,d], D.K. Almutairi [e], J.F. Gómez-Aguilar [f,*], Jehad Alzabut [a,g]

[a] Department of Mathematics and Science, Prince Sultan University, Riyadh 11586, Saudi Arabia
[b] Department of Mathematics, Shaheed Benazir Bhutto University, Dir(U), 18000, Khyber Pakhtunkhwa, Pakistan
[c] Deanship of Graduate Studies and Research, Ahlia University, P.O. Box 10878 Manama, Kingdom of Bahrain
[d] Jadara Research Center, Jadara University, PO Box 733 Irbid, Jordan
[e] Department of Mathematics, College of Science Al-Zulf, Majmaah University, 11952 Al-Majmaah, Saudi Arabia
[f] Centro de Investigación en Ingeniería y Ciencias Aplicadas (CIICAp-IICBA)/UAEM, Universidad Autónoma del Estado de Morelos, Cuernavaca, Mexico
[g] Department of Industrial Engineering, OSTİM Technical University, 06374 Ankara, Türkiye

ARTICLE INFO

Keywords:
Fractal fractional derivative
$\mathscr{CO}_2$ concentration dynamics
Artificial intelligence
Neural networking

ABSTRACT

This research looks into how artificial intelligence (AI) and neural networks (NN) can be used to test data for the input and target driven by mathematical models for the amount of $\mathscr{CO}_2$ in the air. The analysis is carried out within the framework of the fractal-fractional (FF) operator. The work endeavors to design a mathematical model that accurately replicates the levels of $\mathscr{CO}_2$ in response to variables such as human population, forest area, and plantation operations. The paper tries to advance forecasting abilities and establish an enhanced understanding of the intricate dynamics of $\mathscr{CO}_2$ by implementing advanced AI techniques and neural networks. The results of this research add toward advancement in the field of climate change studies as they provide important perspectives for the development of effective measures to reduce $\mathscr{CO}_2$ emissions, subsequently contributing in the fight against global warming and its related repercussions. The AI portion of the article presents the validation and training process for the population of time series data at 1000 epoch with gradient 5.7782×10^{-06}, $\mu = 0.1$ and val fail 0. It shows the model's ability to accurately predict $\mathscr{CO}_2$ concentration dynamics described in (1.1).

1. Introduction

Carbon dioxide ($\mathscr{CO}_2$) is a chemical molecule compound of a single carbon atom that is linked to two oxygen atoms. At regular temperature and pressure, this gas is colorless, denser than air, and cannot ignite fire. $\mathscr{CO}_2$ is widely utilized in various sectors, including the carbonation of drinks, as a chemical precursor, and in firefighting equipment because it has its capacity for replacing oxygen [1,2]. However, its primary impact is in its role as a greenhouse gas, which causes the phenomena of climate change by successfully absorbing heat within the Earth's atmosphere. The effect of greenhouse gases, which is significantly influenced by the increasing levels of atmospheric $\mathscr{CO}_2$ resulting from industrial processes such as fossil fuel combustion and deforestation, plays an important role in discussions about climate change. This effect modifies global climate patterns and contributes to environmental issues like acidification of the seafloor. Precisely controlling and tracking $\mathscr{CO}_2$ emissions, as well as realizing its significance in the carbon cycle, are of critical significance to attaining sustainable development and reducing the adverse impacts of climate change on ecosystems and populations worldwide [3,4].

The global data on emissions of carbon dioxide in recent years explain significant geographical variances related to different business operations and conservation initiatives [5]. According to the data from the world Carbon Project, Asia accounted for 53% of the total world $\mathscr{CO}_2$ emissions in 2022 (Table 1). Out of this, China added 30% and India accounted for 7%. The emissions from China amounted to approximately 10.5 billion metric tons, principally due to coal usage in industry and the production of electricity. On the other hand, India's emissions were approximately 2.8 billion metric tons, mainly coming from the energy and industrial sectors. Europe produced 11% of the total global emissions, with Germany, the UK, and France cumulatively contributing over

* Corresponding author.
E-mail addresses: hkhan@psu.edu.sa (H. Khan), amisaty@gmail.com (M. Abdel-Aty), dk.almutairi@mu.edu.sa (D.K. Almutairi), jose.ga@uaem.mx (J.F. Gómez-Aguilar), jalzabut@psu.edu.sa (J. Alzabut).

https://doi.org/10.1016/j.asej.2025.103460
Received 11 September 2024; Received in revised form 4 April 2025; Accepted 30 April 2025
Available online 21 May 2025

Table 1
Regional Data for the $\mathscr{CO}_2$ During (2017-2021).

Year	Emissions of the $\mathscr{CO}_2$ in BMT	Africa	Asia	North America	Europe	South America
2017	1.5	36.2	11.8	6.5	4.4	2.0
2018	1.6	37.1	12.1	6.9	4.5	2.1
2019	1.7	36.4	12.4	6.6	4.7	2.0
2020	1.8	36.8	12.8	6.4	4.0	2.0
2021	1.9	38.2	13.5	6.8	4.2	2.1

1.7 billion metric tons. The European Union recorded some reductions as a result of strict EU climate laws that encourage the use of renewable energy and energy efficiency. North America, that accounts for 18% of world emissions, witnessed the United States emitting approximately 5 billion metric tons. This demonstrates a decrease in coal consumption but persisting excessive emissions from transportation. Canada and Mexico each provided around 0.6 billion and 0.5 billion metric tons, respectively. Brazil's emissions in South America contributed to about 0.4 billion metric tons, primarily driven by deforestation and agriculture [6,7]. Africa's emissions, constituting roughly 3.8% of the worldwide aggregate, are showing an increase. South Africa, mostly reliant on coal for its energy sector, emits 0.5 billion metric tons. Oceania, spearheaded by Australia, produced over 0.4 billion metric tons of emissions, exhibiting elevated per capita emissions in spite of consumption in renewable energy. The statistical data demonstrates the critical need for measures tailored to specific regions in order to effectively tackle global $\mathscr{CO}_2$ emissions and combat the threat of climate change [8,9].

The images in Fig. 1a through 1f illustrate the variations of $\mathscr{CO}_2$ production and temperature fluctuations over six continents—Asia, Europe, North America, South America, Africa, and Oceania—between 1960 and 2020. Each subplot displays the $\mathscr{CO}_2$ emissions in millions of metric tons, indicated by blue squares on the left y-axis, coupled with the average temperature anomalies in degrees Celsius, expressed by red triangles on the right y-axis. In Asia, there has been a substantial rise in $\mathscr{CO}_2$ emission levels shown in Fig. 1a, growing from 1 million metric tons in 1960 to 18 million metric tons in 2020. The spike in emissions was countered by the rise in temperatures from $0.5\,^{\circ}C$ to $1.2\,^{\circ}C$. Europe discloses a gradual increase in $\mathscr{CO}_2$ emissions initially, attaining high levels in the 1980s, and then seeing a little decline illustrated in Fig. 1b. Meanwhile, temperatures gradually rise from $0.8\,^{\circ}C$ to $1.5\,^{\circ}C$. North America Figuer 1c demonstrates a consistent rise in $\mathscr{CO}_2$ emissions, increasing from 4 to 10 million metric tons, followed by a corresponding temperature elevation from $0.7\,^{\circ}C$ to $1.3\,^{\circ}C$. South America Fig. 1d displays an analogous pattern, with emissions growing from 2 to 8 million metric tons and temperature rising from $0.6\,^{\circ}C$ to $1.2\,^{\circ}C$. Africa and Oceania both exhibit an increasing trend in $\mathscr{CO}_2$ emissions and temperatures, indicating a worldwide pattern of escalating emissions and increasing temperatures. Africa's emissions have risen from 1 to 7 million metric tons, accompanying a temperature rise from $0.5\,^{\circ}C$ to $1.2\,^{\circ}C$ given in Fig. 1e. Similarly, Oceania has noticed a rise in emissions from 2 to 8 million metric tons, along with a temperature increase from $0.6\,^{\circ}C$ to $1.2\,^{\circ}C$. These graphs demonstrate the association between increasing $\mathscr{CO}_2$ concentrations and global temperature rise in Fig. 1f.

Global Warming and $\mathscr{CO}_2$ The climate of the globe is greatly impacted by global warming, that is mainly due to the rising amount of greenhouse gases such as $\mathscr{CO}_2$. In recent decades, there has been a substantial rise in world average temperatures, which has led to in numerous ecological and socioeconomic repercussions [10]. The Table 2 contains a concise summary of significant statistics regarding to the effects due to global warming between the years 2010 and 2020:

The table includes columns for $\mathscr{CO}_2$ emissions (measured in gigatons), global average temperature (measured in degrees Celsius), sea level rise (measured in millimeters per year), and Arctic ice loss (measured as a percentage of ice coverage). These indicators illustrate the multifaceted impacts of global warming on both physical systems and ecosystems. Efforts to address these challenges involve global cooperation, policy initiatives, and technological advancements aimed at reducing emissions and adapting to the changing climate [10–12].

Health issues due to the $\mathscr{CO}_2$**:** The impacts of $\mathscr{CO}_2$ on human health are highlighted in Fig. 2. Though is a necessary component in the human body generated during cellular respiration. However, in excessive amounts, termed to as hypercapnia, may contribute to serious health issues.

From a medical perspective, an excessive amount of $\mathscr{CO}_2$ results in a condition recognized as respiratory acidosis. This condition arises when the blood becomes excessively acidic, leading to symptoms such as headache, dizziness, confusion, and difficulty breathing. Severe cases might lead to neurological consequences such as intense tiredness, seizure disorders, or even a state of unconsciousness. Higher levels of $\mathscr{CO}_2$ also impact the cardiovascular system by causing vasodilation, a process that widens blood vessels. This can result in lowering blood pressure and reduced blood supply to essential organs, which can result in irregular heart rhythms along with various cardiac problems. Continuous elevated levels of $\mathscr{CO}_2$ can hinder the functioning of the respiratory system, resulting in an increase in the rate of breathing. However, continuous exposure to these levels can cause respiratory exhaustion and ultimately respiratory failure, particularly in people who already have illnesses such as chronic obstructive pulmonary disease (COPD). Therefore, it is critical that we sustain optimal levels of $\mathscr{CO}_2$ for the sake of health, demanding medical treatment to avoid serious systemic consequences [12–15].

Importance of dynamical modeling: Modeling and simulations play an important role in different fields, as they provide useful information and help in decision-making processes. Models provide simplified illustrations for complex ecosystems that preserve essential features while removing undesirable components. Simulations include exposing these models to various contexts to analyze their responses. This integration enables researchers and scientists to foresee results, illuminate root causes, and improve performance without the limitations and legal liabilities linked to real-world research [16]. Modeling and simulations have proven crucial in the field of medicine. Their responsibilities include acquiring competence in disease relationships, predicting the occurrence of epidemics, and statistically analyzing the success of treatments [17]. Epidemiological models have shown significant in forecasting the transmission of infectious diseases such as COVID-19 [18,19], Ebola [20], and Zika virus [21], as well as assessing the impact of measures like social isolation and vaccination campaigns. Simulations play an essential part in pharmaceutical research as they assist in estimating the effectiveness and harmful effects, leading to a significant decrease in the time and costs related to these investigations. Modeling and simulations play an essential part in engineering by contributing in designing and assessing of novel products across different industries, such as automobiles and aviation. Simulations play an important part in exposing materials to stress tests, boosting aerodynamics, and improving safety features. This simulated testing environment encourages rapid prototyping and innovation, thus eliminating the demand for costly real models. The discipline of environmental science greatly gains from the application of models to predict the effects of climate change, coordinate conservation efforts, and confirm an environmentally friendly management of ecosystems [22,23]. Economic modeling serves policymakers in forecasting economic trends, assessing fiscal policies, and designing plans for future expansion. The significance of modeling and simulations resides in its capacity to offer a deeper understanding of complex networks, anticipate future possibilities, and establish a suitable and eco-

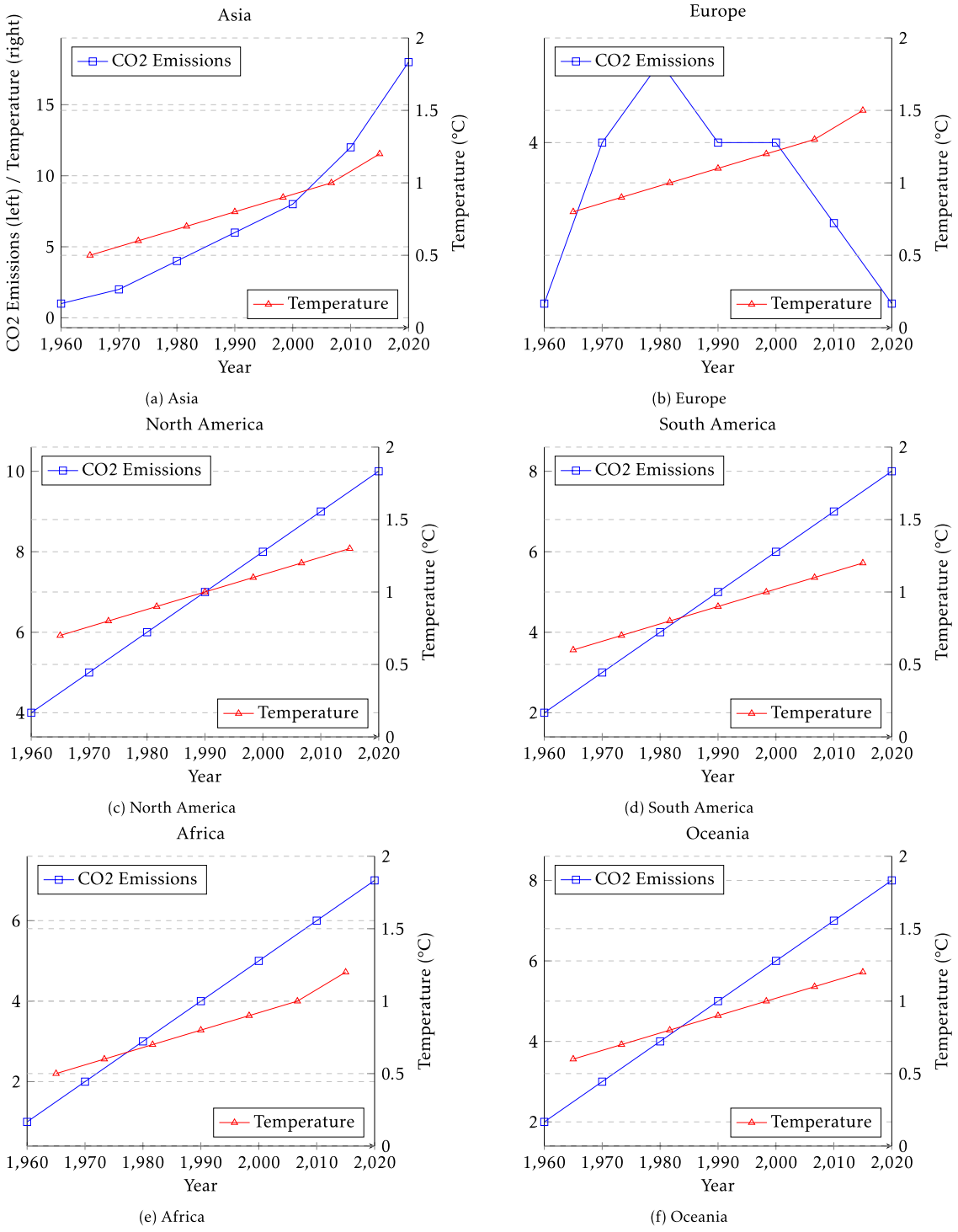

(a) Asia (b) Europe

(c) North America (d) South America

(e) Africa (f) Oceania

Fig. 1. $\mathscr{C}\mathscr{O}_2$ Emissions and Temperature Trends by Continent.

Table 2
Global Warming Statistics.

Year	CO_2 Emissions (GT)	Global Temperature (°C)	Arctic Ice Loss (%)	Sea Level Rise (mm)
2010	32.2	0.6	12	50
2011	33.5	0.7	14	55
2012	34.1	0.8	16	60
2013	34.8	0.9	18	65
2014	35.6	1.0	20	70
2015	36.4	1.1	22	75
2016	37.2	1.2	80	24
2017	38.0	1.3	85	26
2018	39.4	1.4	90	28
2019	40.1	1.5	95	30
2020	41.0	1.6	100	32

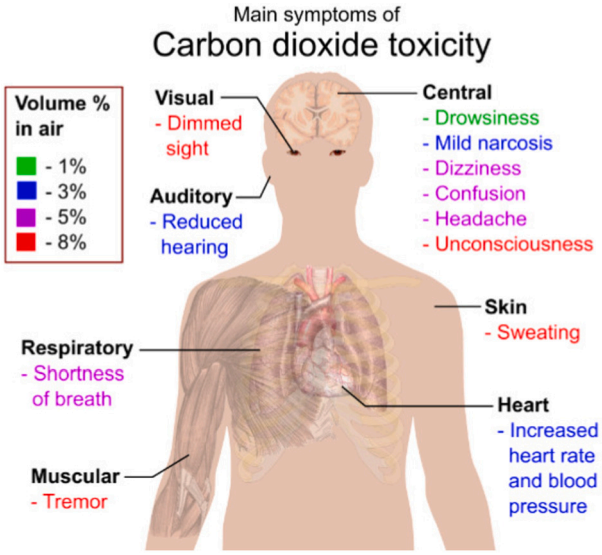

Fig. 2. Impact of $\mathscr{CO}_2$ on human body [15].

nomical atmosphere for testing and innovation. These applications have been extensively utilized across various disciplines, facilitating progress and informed decision-making in healthcare, engineering, environmental science, economics, and other disciplines [24–26].

Artificial intelligence (AI) is transforming the field of disease research by offering sophisticated tools and approaches to comprehend, forecast, and control diverse health issues [27]. AI is having a substantial influence in several important domains:

Predicting Diseases and Detecting Outbreaks AI systems can evaluate large quantities of data, including historical medical information, online social networking activity, and environmental factors, to foresee the development of medical incidents. Machine learning algorithms locate anomalies and patterns that may indicate an imminent outbreak, permitting rapid action [28–30]. During the COVID-19 pandemic, artificial intelligence techniques were utilized to predict increases in cases, offering essential recommendations for public health treatments and resource allocation.

Integration of Multiple Data Sources Artificial intelligence (AI) is highly proficient in combining various datasets, including genomic data, electronic health records, and environmental data, to offer a comprehensive understanding of disease dynamics. This comprehensive approach enables a more profound comprehension of the ways in which different factors contribute to the development and advancement of diseases, resulting in more efficient interventions and policies for public health [31].

AI is revolutionizing the field of disease research by facilitating precise prognostications, tailored therapies, timely identification of health concerns, and streamlined pharmaceutical exploration. The capacity to manage intricate and varied data sources offers priceless insights, facilitating progress in healthcare and enhancing patient outcomes [32,33].

Commands for Neural Network Applications Below are few important MATLAB instructions utilized in the implementation of artificial intelligence to investigate dynamic disease systems [34] 1. **train**: This command is utilized to train a neural network using a designated training methodology. 2. **sim**: This command executes a neural network to assess its effectiveness on input data. 3. The **newff** function generates a forwarding backpropagation network, which is helpful for a range of regression and classification problems. 4. The function "patternnet" is used to generate a pattern recognition network that is specifically designed for solving classification challenges.

FF-$\mathscr{CO}_2$ model and illustration: Atanga [35] introduced a new differential and integral operator called FF-derivative, which combines fractals and fractional calculus. The objective of its construction is to model complex structures using anomalous diffusion processes and fractal-like configurations. Classical calculus falls inadequate when dealing with non-linear and scale-invariant features seen across several disciplines. This is due to how it emphasizes the concept of FF-derivatives [36].

Its ability to precisely represent the impacts of memory and spatial heterogeneity surpasses those of standard derivatives, thereby improving its reliability. The main constraint, however, is the high computing demand and increased mathematical intricacy required to carry out these derivatives [37].

Fractal-fractional derivatives are applied in engineering for signal processing that understand irregular signals and in materials science for the modeling of heterogeneous products. To understand the complex structure of dynamical systems, researchers employed chaotic systems and anomalous diffusion events as defining factors [38–40].

Expanding from the previous research, this paper aims to extend the findings of the study conducted in [42] by employing FF-operators for the analysis of CO_2 data. Various mathematical methodologies have been devised to effectively address the challenges posed by climate change. Using fractal-fractional differentiation to model and study the mathematical dynamics of nonlinear diarrhea transmission dynamics with data This study focuses on modeling the FF order atmospheric carbon dioxide in some regions of Pakistan. We analyze the existence, uniqueness, and stability of the following model.

$$\begin{cases} {}_0^{FFE}D_t^{\mathfrak{r},\mathfrak{r}^{\circledast}}\mathfrak{C}(t) & = \mathfrak{Q} + \lambda N - \alpha\mathfrak{C} - (\lambda_1 + \dfrac{\gamma_1\mathfrak{T}}{K_1+T})\mathfrak{F}\mathfrak{C}, \\ {}_0^{FFE}D_t^{\mathfrak{r},\mathfrak{r}^{\circledast}}\mathcal{N}(t) & = rN(1-\dfrac{N}{K}) + \pi_1\phi N\mathfrak{F} - \theta\mathfrak{C}\mathcal{N}, \\ {}_0^{FFE}D_t^{\mathfrak{r},\mathfrak{r}^{\circledast}}\mathfrak{F}(t) & = u\mathfrak{F}(1-\dfrac{\mathfrak{F}}{M}) - \phi N\mathfrak{F} + \beta\mathfrak{F}\mathfrak{T}, \\ {}_0^{FFE}D_t^{\mathfrak{r},\mathfrak{r}^{\circledast}}\mathfrak{T}(t) & = \upsilon(M-\mathfrak{F}) - \upsilon_0\mathfrak{T}. \end{cases} \tag{1.1}$$

Here, ${}_0^{FFE}D_t^{\mathfrak{r},\mathfrak{r}^{\circledast}}$ represent the fractal fractional derivative the whole population is grouped into four classes. C represents the concentration of $\mathscr{CO}_2$, N is for the humans population in the area, F is for the forest area and T is represents plantation of trees. In model, Q represents the carbon dioxide emission rate naturally, λ is the carbon dioxide emission rate coefficient due to anthropogenic activity, and α is the carbon diox-

Fig. 3. Role of $\mathscr{CO}_2$ in the global warming [41].

ide uptake rate coefficient by natural sinks besides forests, and λ_1 is the rate of carbon dioxide absorption per unit of forest area when no genetically modified trees are present. γ_1 is the utmost amount that may be done with plantations to growth the rate of carbon sequestration per unit of forest area, K_1 is the half-saturation constant, symbolizes plantation exertions where rise CO_2 approval rate is half of its extreme feasible growth that is obtained via the planting of the number trees, r is the basic growing rate, K is carried capability of the people, ϕ is the deforestation, π_1 is the ratio that reflects the increase in the number of people as a result of people using land that has been cleared of trees constant, θ is the population's death rate a function of the deadly impact of climate change brought on by elevated CO_2 levels, u mean the intrinsic growing rate, M means ringing capability of the forest area, β represents the growth rate due to plantation effort, υ means the employment rate and υ_0 represents the declination rate coefficient of the manor efforts. The model is considered in FF sense of fractional derivative with the help of [35,36].

Definition 1.1. Suppose $\psi(\mathfrak{t})$ is a continues function and fractal differentiable in the interval (a,b) of order $\mathfrak{r}^{\circledast}$, then the fractal fractional derivative of $\psi\mathfrak{t}$ of order $\mathfrak{r}\in(0,1)$ in the caputo sense is given by: ${}^{FF}{}_0D_{\mathfrak{t}}^{\mathfrak{r},\mathfrak{r}^{\circledast}}\psi=\frac{\mathscr{G}(\mathfrak{r})}{1-\mathfrak{r}}\int_0^{\mathfrak{t}}\frac{d}{d\mathfrak{t}^{\mathfrak{r}^{\circledast}}}E_{g_1}\left(-\frac{\mathfrak{r}}{1-\mathfrak{r}}(\mathfrak{t}-s)^{\mathfrak{r}}\right)\psi(s)ds.$

Definition 1.2. Suppose ψ is continues function in the interval (a, b) then the FF integral of ψ of order $\mathfrak{r}$ having ML type kernal is given by ${}^{FF}{}_0I_{\mathfrak{t}}^{\mathfrak{r},\mathfrak{r}^{\circledast}}\psi=\frac{\mathfrak{r}\mathfrak{r}^{\circledast}}{\mathscr{G}(\mathfrak{r})\Gamma\mathfrak{r}}\int_0^{\mathfrak{t}}s^{\mathfrak{r}^{\circledast}-1}\psi(s)(\mathfrak{t}-s)^{\mathfrak{r}-1}ds+\frac{\mathfrak{r}^{\circledast}(1-\mathfrak{r})\mathfrak{t}^{(\mathfrak{r}^{\circledast}-1)}}{\mathscr{G}(\mathfrak{r})}\psi$, where $\mathscr{G}(\mathfrak{r})=1-\mathfrak{r}+\frac{\mathfrak{r}}{\Gamma\mathfrak{r}}$.

In the upcoming mathematical expressions, we will use $\mathscr{U}(\mathfrak{t},s)=s^{\mathfrak{r}^{\circledast}-1}(\mathfrak{t}-s)^{\mathfrak{r}-1}$, for simplicity. We define a Banach space of $\mathscr{B}=\{u\in C([0,T]:\mathbb{R})\}$, with a norm $\|u\|=\max_{\mathfrak{t}\in I_{[0,T]}}|u(\mathfrak{t})|$.

2. Existence criteria

With the help of fixed point procedure, we check the existence of FF–$\mathscr{CO}_2$ concentration dynamics (1.1), we have

$$\begin{cases}\mathfrak{C}(\mathfrak{t})-\mathfrak{C}(0) &= \frac{\mathfrak{r}\mathfrak{r}^{\circledast}}{\mathscr{G}(\mathfrak{r})\Gamma\mathfrak{r}}\int_0^{\mathfrak{t}}\mathscr{U}(\mathfrak{t},s)(\mathfrak{Q}+\lambda\mathcal{N}-\alpha\mathfrak{C}-(\lambda_1+\frac{\gamma_1T}{K_1+T})\mathfrak{F}\mathfrak{C})ds\\ &\quad+\frac{\mathfrak{r}^{\circledast}(1-\mathfrak{r})\mathfrak{t}^{\mathfrak{r}^{\circledast}-1}}{\mathscr{G}(\mathfrak{r})}(\mathfrak{Q}+\lambda\mathcal{N}-\alpha\mathfrak{C}-(\lambda_1+\frac{\gamma_1T}{K_1+T})\mathfrak{F}\mathfrak{C}),\\ \mathcal{N}(\mathfrak{t})-\mathcal{N}(0) &= \frac{\mathfrak{r}\mathfrak{r}^{\circledast}}{\mathscr{G}(\mathfrak{r})\Gamma\mathfrak{r}}\int_0^{\mathfrak{t}}\mathscr{U}(\mathfrak{t},s)(r\mathcal{N}(1-\frac{\mathcal{N}}{K})+\pi_1\phi\mathcal{N}\mathfrak{F}-\theta\mathfrak{C}\mathcal{N})ds\\ &\quad+\frac{\mathfrak{r}^{\circledast}(1-\mathfrak{r})\mathfrak{t}^{\mathfrak{r}^{\circledast}-1}}{\mathscr{G}(\mathfrak{r})}(r\mathcal{N}(1-\frac{\mathcal{N}}{K})+\pi_1\phi\mathcal{N}\mathfrak{F}-\theta\mathfrak{C}\mathcal{N}),\\ \mathfrak{F}(\mathfrak{t})-\mathfrak{F}(0) &= \frac{\mathfrak{r}\mathfrak{r}^{\circledast}}{\mathscr{G}(\mathfrak{r})\Gamma\mathfrak{r}}\int_0^{\mathfrak{t}}\mathscr{U}(\mathfrak{t},s)(u\mathfrak{F}(1-\frac{\mathfrak{F}}{M})-\phi N\mathfrak{F}+\beta\mathfrak{F}\mathfrak{T})ds\\ &\quad+\frac{\mathfrak{r}^{\circledast}(1-\mathfrak{r})\mathfrak{t}^{\mathfrak{r}^{\circledast}-1}}{\mathscr{G}(\mathfrak{r})}(u\mathfrak{F}(1-\frac{\mathfrak{F}}{M})-\phi\mathcal{N}\mathfrak{F}+\beta\mathfrak{F}\mathfrak{T}),\\ \mathfrak{T}(\mathfrak{t})-\mathfrak{T}(0) &= \frac{\mathfrak{r}\mathfrak{r}^{\circledast}}{\mathscr{G}(\mathfrak{r})\Gamma\mathfrak{r}}\int_0^{\mathfrak{t}}\mathscr{U}(\mathfrak{t},s)(\upsilon(M-\mathfrak{F})-\upsilon_0\mathfrak{T})ds\\ &\quad+\frac{\mathfrak{r}^{\circledast}(1-\mathfrak{r})\mathfrak{t}^{\mathfrak{r}^{\circledast}-1}}{\mathscr{G}(\mathfrak{r})}(\upsilon(M-\mathfrak{F})-\upsilon_0\mathfrak{T}).\end{cases}\tag{2.1}$$

Now, we define some functions $\mathfrak{Q}_i$ and some constants ψ_i, $i\epsilon N_1^4$, for the main results of the paper.

$$\begin{cases}\mathscr{H}_1(\mathfrak{t},\mathfrak{C}) &= \mathfrak{Q}+\lambda\mathcal{N}-\alpha\mathfrak{C}-(\lambda_1+\frac{\gamma_1T}{K_1+T})\mathfrak{F}\mathfrak{C},\\ \mathscr{H}_2(\mathfrak{t},\mathcal{N}) &= r\mathcal{N}(1-\frac{\mathcal{N}}{K})+\pi_1\phi\mathcal{N}\mathfrak{F}-\theta\mathfrak{C}\mathcal{N},\\ \mathscr{H}_3(\mathfrak{t},\mathfrak{F}) &= u\mathfrak{F}(1-\frac{\mathfrak{F}}{M})-\phi N\mathfrak{F}+\beta\mathfrak{F}\mathfrak{T},\\ \mathscr{H}_4(\mathfrak{t},\mathfrak{T}) &= \upsilon(M-\mathfrak{F})-\upsilon_0\mathfrak{T}.\end{cases}\tag{2.2}$$

$(\mathscr{K}^{\circledast})$: We assume the boundedness of the functions $\mathfrak{C}(\mathfrak{t})$, $\mathcal{N}(\mathfrak{t})$, $\mathfrak{F}(\mathfrak{t})$, $\mathfrak{T}(\mathfrak{t})$ and $\mathfrak{C}^{\circledast}(\mathfrak{t})$, $\mathcal{N}^{\circledast}(\mathfrak{t})$, $\mathfrak{F}^{\circledast}(\mathfrak{t})$, $\mathfrak{T}^{\circledast}(\mathfrak{t})$ all belongs to $L[0,1]$ with $\|\mathcal{N}\|\le\psi_1$, $\|\mathfrak{T}\|\le\psi_2$, $\|\mathfrak{F}\|\le\psi_3$, and $\|\mathfrak{C}\|\le\psi_4$ for some $\psi_i\ge0$, $i=1,2,3,4$.

Theorem 2.1. *The kernals $\mathscr{H}_1$, $\mathscr{H}_2$, $\mathscr{H}_3$, $\mathscr{H}_4$ are satisfying LC if $(\mathscr{K}^{\circledast})$ holds true and satisfy $\phi_i<1$ for $i\in N_1^4$.*

Proof. First, we show that $\mathscr{H}_1(\mathfrak{t},\mathfrak{C})$ obeys LC, for this, consider

$$\begin{aligned}|\mathscr{H}_1(\mathfrak{t},\mathfrak{C})-\mathscr{H}_1(\mathfrak{t},\mathfrak{C}^{\circledast})| &= \|\mathfrak{Q}+\lambda\mathcal{N}-\alpha\mathfrak{C}-(\lambda_1+\frac{\gamma_1T}{K_1+T})\mathfrak{F}\mathfrak{C}\\ &\quad-(\mathfrak{Q}+\lambda\mathcal{N}-\alpha\mathfrak{C}^{\circledast}-(\lambda_1+\frac{\gamma_1T}{K_1+T})\mathfrak{F}\mathfrak{C}^{\circledast})\\ &= \|\alpha(\mathfrak{C}^{\circledast}-\mathfrak{C})+(\lambda_1+\gamma_1\psi_2)(\mathfrak{C}^{\circledast}-\mathfrak{C})\|\\ &\le(\alpha+\lambda_1+\gamma_1\psi_2)\|(\mathfrak{C}^{\circledast}-\mathfrak{C})\|\\ &\le\phi_1\|(\mathfrak{C}^{\circledast}-\mathfrak{C})\|,\end{aligned}$$

where $\phi_1 = \alpha + \lambda_1 + \gamma_1\psi_2$. Hence $\mathscr{H}_1$ satisfies LC and $\phi_1 < 1$. Similarly, we can reach to the situation that $\mathscr{H}_2(t, \mathcal{N})$ satisfies the LC with constant $\phi_2 = r + \frac{2r\psi_1}{k} + \pi_1\phi\psi_3 + \theta\psi_4$, where $\phi_2 < 1$. Furthermore, we have $\phi_3 = u(1 + \frac{2\psi_3}{M}) + \phi\psi_1 + \beta\psi_2$, $\phi_4 = \upsilon_0$, with both the $\phi_3 < 1$ and $\phi_4 < 1$, which implies $\mathscr{H}_3$ and $\mathscr{H}_4$ do satisfy the LC. Hence, all the $\mathscr{H}_i$, for $i = 1, 2, 3, 4$, fulfill LCs and for $\phi_i < 1$ for $i \in N_1^4$, they are contractions. □

We rewrite the system of equations from (2.1) in the following form by using the kernals $\mathscr{H}_i$, $i \in N_1^4$, we have

$$\begin{cases} \mathfrak{C}(t) &= \mathfrak{C}(0) + \frac{\mathfrak{r}\mathfrak{r}^{\circledast}}{\mathscr{G}(\mathfrak{r})\Gamma\mathfrak{r}} \int_0^t \mathscr{U}(t,s)\mathscr{H}_1(s,\mathfrak{C}(s))ds \\ &\quad + \frac{\mathfrak{r}^{\circledast}(1-\mathfrak{r})t^{\mathfrak{r}^{\circledast}-1}}{\mathscr{G}(\mathfrak{r})}\mathscr{H}_1(t,\mathfrak{C}(t)), \\ \mathcal{N}(t) &= \mathcal{N}(0) + \frac{\mathfrak{r}\mathfrak{r}^{\circledast}}{\mathscr{G}(\mathfrak{r})\Gamma\mathfrak{r}} \int_0^t \mathscr{U}(t,s)\mathscr{H}_2(s,\mathcal{N}(s))ds \\ &\quad + \frac{\mathfrak{r}^{\circledast}(1-\mathfrak{r})t^{\mathfrak{r}^{\circledast}-1}}{\mathscr{G}(\mathfrak{r})}\mathscr{H}_2(t,\mathcal{N}(t)), \\ \mathfrak{F}(t) &= \mathfrak{F}(0) + \frac{\mathfrak{r}\mathfrak{r}^{\circledast}}{\mathscr{G}(\mathfrak{r})\Gamma\mathfrak{r}} \int_0^t \mathscr{U}(t,s)\mathscr{H}_3(s,\mathfrak{F}(s))ds \\ &\quad + \frac{\mathfrak{r}^{\circledast}(1-\mathfrak{r})t^{\mathfrak{r}^{\circledast}-1}}{\mathscr{G}(\mathfrak{r})}\mathscr{H}_3(t,\mathfrak{F}(t)), \\ \mathfrak{T}(t) &= \mathfrak{T}(0) + \frac{\mathfrak{r}\mathfrak{r}^{\circledast}}{\mathscr{G}(\mathfrak{r})\Gamma\mathfrak{r}} \int_0^t \mathscr{U}(t,s)\mathscr{H}_4(s,\mathfrak{T}(s))ds \\ &\quad + \frac{\mathfrak{r}^{\circledast}(1-\mathfrak{r})t^{\mathfrak{r}^{\circledast}-1}}{\mathscr{G}(\mathfrak{r})}\mathscr{H}_4(t,\mathfrak{T}(t)). \end{cases} \tag{2.3}$$

We proceed to the iterative scheme

$$\mathfrak{C}_n(t) = \mathfrak{C}(0) + \frac{\mathfrak{r}\mathfrak{r}^{\circledast}}{\mathscr{G}(\mathfrak{r})\Gamma\mathfrak{r}} \int_0^t \mathscr{U}(t,s)\mathscr{H}_1(s,\mathfrak{C}_{n-1}(s))ds + \frac{\mathfrak{r}^{\circledast}(1-\mathfrak{r})t^{\mathfrak{r}^{\circledast}-1}}{\mathscr{G}(\mathfrak{r})}\mathscr{H}_1(t,\mathfrak{C}_{n-1}(t)),$$

$$\mathcal{N}_n(t) = \mathcal{N}(0) + \frac{\mathfrak{r}\mathfrak{r}^{\circledast}}{\mathscr{G}(\mathfrak{r})\Gamma\mathfrak{r}} \int_0^t \mathscr{U}(t,s)\mathscr{H}_2(s,\mathcal{N}_{n-1}(s))ds + \frac{\mathfrak{r}^{\circledast}(1-\mathfrak{r})t^{\mathfrak{r}^{\circledast}-1}}{\mathscr{G}(\mathfrak{r})}\mathscr{H}_2(t,\mathcal{N}_{n-1}(t)),$$

$$\mathfrak{F}_n(t) = \mathfrak{F}(0) + \frac{\mathfrak{r}\mathfrak{r}^{\circledast}}{\mathscr{G}(\mathfrak{r})\Gamma\mathfrak{r}} \int_0^t \mathscr{U}(t,s)\mathscr{H}_3(s,\mathfrak{F}_{n-1}(s))ds + \frac{\mathfrak{r}^{\circledast}(1-\mathfrak{r})t^{\mathfrak{r}^{\circledast}-1}}{\mathscr{G}(\mathfrak{r})}\mathscr{H}_3(t,\mathfrak{F}_{n-1}(t)),$$

$$\mathfrak{T}_n(t) = \mathfrak{T}(0) + \frac{\mathfrak{r}\mathfrak{r}^{\circledast}}{\mathscr{G}(\mathfrak{r})\Gamma\mathfrak{r}} \int_0^t \mathscr{U}(t,s)\mathscr{H}_4(s,\mathfrak{T}_{n-1}(s))ds + \frac{\mathfrak{r}^{\circledast}(1-\mathfrak{r})t^{\mathfrak{r}^{\circledast}-1}}{\mathscr{G}(\mathfrak{r})}\mathscr{H}_4(t,\mathfrak{T}_{n-1}(t)).$$

Theorem 2.2. *Under the consideration of hypothesis* ($\mathscr{K}^{\circledast}$), *the FF–$\mathscr{CO}_2$ concentration dynamics* (1.1) *has a solution provided that* $\sigma = \max\{\phi_i\} < 1$, *for* $i = 1, 2, ..., 4$.

Proof. Let us define the following functions:

$$\begin{cases} \mathscr{P}_1 n(t) &= \mathfrak{C}_{n+1}(t) - \mathfrak{C}(t), \\ \mathscr{P}_2 n(t) &= \mathcal{N}_{n+1}(t) - \mathcal{N}(t), \\ \mathscr{P}_3 n(t) &= \mathcal{F}_{n+1}(t) - \mathfrak{F}(t), \\ \mathscr{P}_4 n(t) &= \mathcal{T}_{n+1}(t) - \mathfrak{T}(t). \end{cases} \tag{2.4}$$

Taking norm of the system (2.4) we have

$$\begin{aligned} &\|\mathscr{P}_{1_n}\| \\ &= \|\mathfrak{C}_{n+1}(t) - \mathfrak{C}(t)\| \\ &= \left\| \frac{\mathfrak{r}\mathfrak{r}^{\circledast}}{\mathscr{G}(\mathfrak{r})\Gamma\mathfrak{r}} \int_0^t \mathscr{U}(t,s)\mathscr{H}_1(s,\mathfrak{C}_n(s))ds + \frac{\mathfrak{r}^{\circledast}(1-\mathfrak{r})t^{\mathfrak{r}^{\circledast}-1}}{\mathscr{G}(\mathfrak{r})}\mathscr{H}_1(t,\mathfrak{C}_n(t)) \right. \\ &\quad \left. - \left(\frac{\mathfrak{r}\mathfrak{r}^{\circledast}}{\mathscr{G}(\mathfrak{r})\Gamma\mathfrak{r}} \int_0^t \mathscr{U}(t,s)\mathscr{H}_1(s,\mathfrak{C}(s))ds + \frac{\mathfrak{r}^{\circledast}(1-\mathfrak{r})t^{\mathfrak{r}^{\circledast}-1}}{\mathscr{G}(\mathfrak{r})}\mathscr{H}_1(t,\mathfrak{C}(t)) \right) \right\| \\ &= \frac{\mathfrak{r}\mathfrak{r}^{\circledast}}{\mathscr{G}(\mathfrak{r})\Gamma\mathfrak{r}} \int_0^t \mathscr{U}(t,s)\|\mathscr{H}_1(s,\mathfrak{C}_n(s)) - \mathscr{H}_1(s,\mathfrak{C}(s))\|ds \\ &\quad + \frac{\mathfrak{r}^{\circledast}(1-\mathfrak{r})t^{\mathfrak{r}^{\circledast}-1}}{\mathscr{G}(\mathfrak{r})}\|\mathscr{H}_1(t,\mathfrak{C}_n(t)) - \mathscr{H}_1(t,\mathfrak{C}(t))\| \\ &\leq \left(\frac{\mathfrak{r}\mathfrak{r}^{\circledast}}{\mathscr{G}(\mathfrak{r})\Gamma\mathfrak{r}} \int_0^t \mathscr{U}(t,s)ds + \frac{\mathfrak{r}^{\circledast}(1-\mathfrak{r})t^{\mathfrak{r}^{\circledast}-1}}{\mathscr{G}(\mathfrak{r})} \right)\phi_1\|\mathfrak{C}_n - \mathfrak{C}\| \\ &\leq \left(\frac{\mathfrak{r}\mathfrak{r}^{\circledast}\Gamma\mathfrak{r}^{\circledast}}{\mathscr{G}(\mathfrak{r})\Gamma(\mathfrak{r}+\mathfrak{r}^{\circledast}))} + \frac{\mathfrak{r}^{\circledast}(1-\mathfrak{r})}{\mathscr{G}(\mathfrak{r})} \right)\phi_1\|\mathfrak{C}_n - \mathfrak{C}\| \\ &\leq \left(\frac{\mathfrak{r}\mathfrak{r}^{\circledast}\Gamma\mathfrak{r}^{\circledast}}{\mathscr{G}(\mathfrak{r})\Gamma(\mathfrak{r}+\mathfrak{r}^{\circledast}))} + \frac{\mathfrak{r}^{\circledast}(1-\mathfrak{r})}{\mathscr{G}(\mathfrak{r})} \right)^n \sigma^n\|\mathfrak{C}_1 - \mathfrak{C}\|, \end{aligned}$$

where $\sigma < 1$ and as $n \to \infty$ so $\mathfrak{C}_n \to \mathfrak{C}$ and using the formula $B(u,v) = (b-a)^{-u+v+1}\int_a^b (s-a)^{u-1}(b-s)^{v-1}ds$ and as $t \in [0,1]$ so $t^{-1-\mathfrak{r}+\mathfrak{r}^{\circledast}} \leq 1$ and $t^{\mathfrak{r}^{\circledast}} \leq 1$. Similarly, we have $\|\mathcal{N}_{n+1} - \mathcal{N}\| \leq \left(\frac{\mathfrak{r}\mathfrak{r}^{\circledast}\Gamma\mathfrak{r}^{\circledast}}{\mathscr{G}(\mathfrak{r})\Gamma(\mathfrak{r}+\mathfrak{r}^{\circledast}))} + \frac{\mathfrak{r}^{\circledast}(1-\mathfrak{r})}{\mathscr{G}(\mathfrak{r})} \right)^n \sigma^n\|\mathcal{N}_1 - \mathcal{N}\|$, and $\sigma < 1$, implies that, as $n \to \infty$, so $\mathcal{N}_n \to \mathcal{N}$. Also, for the $\mathfrak{F}$ and $\mathfrak{T}$, we have that, as $n \to \infty$, then $\mathfrak{F}_n \to \mathfrak{F}$, $\mathfrak{T}_n \to \mathfrak{T}$. Consequently, the FF–$\mathscr{CO}_2$ concentration dynamics (1.1), has a solution. □

Theorem 2.3. *Under the consideration of hypothesis* ($\mathscr{K}^{\circledast}$), *the uniqueness of solution for the FF–$\mathscr{CO}_2$ concentration dynamics* (1.1) *is satisfied provided that:* $\left(\frac{\mathfrak{r}\mathfrak{r}^{\circledast}\Gamma\mathfrak{r}^{\circledast}}{\mathscr{G}(\mathfrak{r})\Gamma(\mathfrak{r}+\mathfrak{r}^{\circledast}))} + \frac{\mathfrak{r}^{\circledast}(1-\mathfrak{r})}{\mathscr{G}(\mathfrak{r})} \right)\phi_i \leq 1$, $i \in N_1^4$

Proof. Following a contradiction of the uniqueness of solution of the presumed FF–$\mathscr{CO}_2$ concentration dynamics (1.1), such that $\mathfrak{C}^{\circledast}$, $\mathcal{N}^{\circledast}$, $\mathfrak{F}^{\circledast}$, $\mathfrak{T}^{\circledast}$, satisfying the given model. We have

$$\mathfrak{C}^{\circledast}(t) = \frac{\mathfrak{r}\mathfrak{r}^{\circledast}}{\mathscr{G}(\mathfrak{r})\Gamma\mathfrak{r}} \int_0^t \mathscr{U}(t,s)\mathscr{H}_1(s,\mathfrak{C}^{\circledast}(s))ds + \frac{\mathfrak{r}^{\circledast}(1-\mathfrak{r})t^{\mathfrak{r}^{\circledast}-1}}{\mathscr{G}(\mathfrak{r})}\mathscr{H}_1(t,\mathfrak{C}^{\circledast}(t)),$$

$$\mathcal{N}^{\circledast}(t) = \frac{\mathfrak{r}\mathfrak{r}^{\circledast}}{\mathscr{G}(\mathfrak{r})\Gamma\mathfrak{r}} \int_0^t \mathscr{U}(t,s)\mathscr{H}_2(s,\mathcal{N}^{\circledast}(s))ds + \frac{\mathfrak{r}^{\circledast}(1-\mathfrak{r})t^{\mathfrak{r}^{\circledast}-1}}{\mathscr{G}(\mathfrak{r})}\mathscr{H}_2(t,\mathcal{N}^{\circledast}(t)),$$

$$\mathfrak{F}^{\circledast}(t) = \frac{\mathfrak{r}\mathfrak{r}^{\circledast}}{\mathscr{G}(\mathfrak{r})\Gamma\mathfrak{r}} \int_0^t \mathscr{U}(t,s)\mathscr{H}_3(s,\mathfrak{F}^{\circledast}(s))ds + \frac{\mathfrak{r}^{\circledast}(1-\mathfrak{r})t^{\mathfrak{r}^{\circledast}-1}}{\mathscr{G}(\mathfrak{r})}\mathscr{H}_3(t,\mathfrak{F}^{\circledast}(t)),$$

$$\mathfrak{T}^{\circledast}(t) = \frac{\mathfrak{r}\mathfrak{r}^{\circledast}}{\mathscr{G}(\mathfrak{r})\Gamma\mathfrak{r}} \int_0^t \mathscr{U}(t,s)\mathscr{H}_4(s,\mathfrak{T}^{\circledast}(s))ds + \frac{\mathfrak{r}^{\circledast}(1-\mathfrak{r})t^{\mathfrak{r}^{\circledast}-1}}{\mathscr{G}(\mathfrak{r})}\mathscr{H}_4(t,\mathfrak{T}^{\circledast}(t)).$$

Now taking norm of the difference of both the solutions

$$
\begin{aligned}
|\mathfrak{C}(\mathfrak{t})-\mathfrak{C}^{\circledast}(\mathfrak{t})| &= \Bigg\| \Bigg(\frac{\mathfrak{r}\mathfrak{r}^{\circledast}}{\mathcal{G}(\mathfrak{r})\Gamma\mathfrak{r}} \int_0^{\mathfrak{t}} \mathcal{U}(\mathfrak{t},s)\mathscr{H}_1(s,\mathfrak{C}(s))ds \\
&+ \frac{\mathfrak{r}^{\circledast}(1-\mathfrak{r})\mathfrak{t}^{\mathfrak{r}^{\circledast}-1}}{\mathcal{G}(\mathfrak{r})}\mathscr{H}_1(\mathfrak{t},\mathfrak{C}(\mathfrak{t}))\Bigg) \\
&- \Bigg(\frac{\mathfrak{r}\mathfrak{r}^{\circledast}}{\mathcal{G}(\mathfrak{r})\Gamma\mathfrak{r}} \int_0^{\mathfrak{t}} \mathcal{U}(\mathfrak{t},s)\mathscr{H}_1(s,\mathfrak{C}^{\circledast}(s))ds \\
&+ \frac{\mathfrak{r}^{\circledast}(1-\mathfrak{r})\mathfrak{t}^{\mathfrak{r}^{\circledast}-1}}{\mathcal{G}(\mathfrak{r})}\mathscr{H}_1(\mathfrak{t},\mathfrak{C}^{\circledast}(\mathfrak{t}))\Bigg)\Bigg\| \\
&= \frac{\mathfrak{r}\mathfrak{r}^{\circledast}}{\mathcal{G}(\mathfrak{r})\Gamma\mathfrak{r}} \int_0^{\mathfrak{t}} \mathcal{U}(\mathfrak{t},s)\|\mathscr{H}_1(s,\mathfrak{C}(s)-\mathscr{H}_1(s,\mathfrak{C}^{\circledast}(s))\|ds \\
&+ \frac{\mathfrak{r}^{\circledast}(1-\mathfrak{r})\mathfrak{t}^{\mathfrak{r}^{\circledast}-1}}{\mathcal{G}(\mathfrak{r})}\|\mathscr{H}_1(\mathfrak{t},\mathfrak{C}(\mathfrak{t})-\mathscr{H}_1(\mathfrak{t},\mathfrak{C}^{\circledast}(\mathfrak{t}))\|ds \\
&\leq \Bigg(\frac{\mathfrak{r}\mathfrak{r}^{\circledast}}{\mathcal{G}(\mathfrak{r})\Gamma\mathfrak{r}} \int_0^{\mathfrak{t}} \mathcal{U}(\mathfrak{t},s) \\
&+ \frac{\mathfrak{r}^{\circledast}(1-\mathfrak{r})\mathfrak{t}^{\mathfrak{r}^{\circledast}-1}}{\mathcal{G}(\mathfrak{r})}\Bigg)\phi_1\|\mathfrak{C}-\mathfrak{C}^{\circledast}\|, \\
&\Longrightarrow \Bigg[1-\Bigg(\frac{\mathfrak{r}\mathfrak{r}^{\circledast}\Gamma\mathfrak{r}^{\circledast}}{\mathcal{G}(\mathfrak{r})\Gamma(\mathfrak{r}+\mathfrak{r}^{\circledast}))} \\
&+ \frac{\mathfrak{r}^{\circledast}(1-\mathfrak{r})}{\mathcal{G}(\mathfrak{r})}\Bigg)\phi_1\Bigg]\|\mathfrak{C}-\mathfrak{C}^{\circledast}\| \leq 0. \qquad (2.5)
\end{aligned}
$$

This is possible for $\|\mathfrak{C}-\mathfrak{C}^{\circledast}\|=0$, or equivalently, $\mathfrak{C}=\mathfrak{C}^{\circledast}$. This confirms the uniqueness for the $\mathfrak{C}$. Similarly, for $\mathcal{N}$, we have $\Bigg[1-\Bigg(\frac{\mathfrak{r}\mathfrak{r}^{\circledast}\Gamma\mathfrak{r}^{\circledast}}{\mathcal{G}(\mathfrak{r})\Gamma(\mathfrak{r}+\mathfrak{r}^{\circledast}))}+\frac{\mathfrak{r}^{\circledast}(1-\mathfrak{r})}{\mathcal{G}(\mathfrak{r})}\Bigg)\phi_2\Bigg]\|\mathcal{N}-\mathcal{N}^{\circledast}\|\leq 0$, which implies $\mathcal{N}=\mathcal{N}^{\circledast}$. For the other two classes of the FF–$\mathscr{C}\mathscr{O}_2$ concentration dynamics (1.1), we have $\mathfrak{F}=\mathfrak{F}^{\circledast}$, $\mathfrak{T}=\mathfrak{T}^{\circledast}$. Thus, the uniqueness of the solution of FF–$\mathscr{C}\mathscr{O}_2$ concentration dynamics (1.1) is proved. □

Definition 2.4. The FF-integral system (2.3) is said to be generalized HUR-stable if for each solution $(\mathfrak{C},\mathcal{N},\mathfrak{F},\mathfrak{T})\in\mathscr{B}^4$, there exit constants $\delta_k>0$, $k\in N_1^4$, and for $\zeta_i>0$, $i\in N_1^4$, we have

$$
\begin{aligned}
&\Bigg|\mathfrak{C}(\mathfrak{t})-\frac{\mathfrak{r}\mathfrak{r}^{\circledast}}{\mathcal{G}(\mathfrak{r})\Gamma\mathfrak{r}}\int_0^{\mathfrak{t}}\mathcal{U}(\mathfrak{t},s)\mathscr{H}_1(s,\mathfrak{C}(s))ds-\frac{\mathfrak{r}^{\circledast}(1-\mathfrak{r})\mathfrak{t}^{\mathfrak{r}^{\circledast}-1}}{\mathcal{G}(\mathfrak{r})}\mathscr{H}_1(\mathfrak{t},\mathfrak{C}(\mathfrak{t}))\Bigg| \\
&\leq\zeta_1, \\
&\Bigg|\mathcal{N}(\mathfrak{t})-\frac{\mathfrak{r}\mathfrak{r}^{\circledast}}{\mathcal{G}(\mathfrak{r})\Gamma\mathfrak{r}}\int_0^{\mathfrak{t}}\mathcal{U}(\mathfrak{t},s)\mathscr{H}_2(s,\mathcal{N}(s))ds-\frac{\mathfrak{r}^{\circledast}(1-\mathfrak{r})\mathfrak{t}^{\mathfrak{r}^{\circledast}-1}}{\mathcal{G}(\mathfrak{r})}\mathscr{H}_2(\mathfrak{t},\mathcal{N}(\mathfrak{t}))\Bigg| \\
&\leq\zeta_2, \\
&\Bigg|\mathfrak{F}(\mathfrak{t})-\frac{\mathfrak{r}\mathfrak{r}^{\circledast}}{\mathcal{G}(\mathfrak{r})\Gamma\mathfrak{r}}\int_0^{\mathfrak{t}}\mathcal{U}(\mathfrak{t},s)\mathscr{H}_3(s,\mathfrak{F}(s))ds-\frac{\mathfrak{r}^{\circledast}(1-\mathfrak{r})\mathfrak{t}^{\mathfrak{r}^{\circledast}-1}}{\mathcal{G}(\mathfrak{r})}\mathscr{H}_3(\mathfrak{t},\mathfrak{F}(\mathfrak{t}))\Bigg| \\
&\leq\zeta_3, \\
&\Bigg|\mathfrak{T}(\mathfrak{t})-\frac{\mathfrak{r}\mathfrak{r}^{\circledast}}{\mathcal{G}(\mathfrak{r})\Gamma\mathfrak{r}}\int_0^{\mathfrak{t}}\mathcal{U}(\mathfrak{t},s)\mathscr{H}_4(s,\mathfrak{T}(s))ds-\frac{\mathfrak{r}^{\circledast}(1-\mathfrak{r})\mathfrak{t}^{\mathfrak{r}^{\circledast}-1}}{\mathcal{G}(\mathfrak{r})}\mathscr{H}_4(\mathfrak{t},\mathfrak{T}(\mathfrak{t}))\Bigg| \\
&\leq\zeta_4.
\end{aligned}
$$

There exists a solution $(\mathfrak{C}^{\circledast},\mathcal{N}^{\circledast},\mathfrak{F}^{\circledast},\mathfrak{T}^{\circledast})\in\mathscr{B}^4$ of the FF–$\mathscr{C}\mathscr{O}_2$ concentration dynamics (1.1), satisfying that

$$
\begin{aligned}
&|\mathfrak{C}(\mathfrak{t})-\mathfrak{C}^{\circledast}(\mathfrak{t})|\leq\delta_1\zeta_1, \\
&|\mathcal{N}(\mathfrak{t})-\mathcal{N}^{\circledast}(\mathfrak{t})|\leq\delta_2\zeta_2, \\
&\mathfrak{F}(\mathfrak{t})-\mathfrak{F}^{\circledast}(\mathfrak{t})|\leq\delta_3\zeta_3, \qquad (2.6) \\
&|\mathfrak{T}(\mathfrak{t})-\mathfrak{T}^{\circledast}(\mathfrak{t})|\leq\delta_4\zeta_4.
\end{aligned}
$$

Definition 2.5. The FF-integral system (2.3) is said to be generalized HUR-stable with respect to $\mathscr{T}_j(\mathfrak{t})$, where $j\in\{1,2,3,4\}$, if for each solution $(\mathfrak{C},\mathcal{N},\mathfrak{F},\mathfrak{T})\in\mathscr{B}^4$, there exit constants $\delta_k^{\circledast}>0$, $k\in N_1^4$, with

$$
\begin{aligned}
&\Bigg|\mathfrak{C}(\mathfrak{t})-\frac{\mathfrak{r}\mathfrak{r}^{\circledast}}{\mathcal{G}(\mathfrak{r})\Gamma\mathfrak{r}}\int_0^{\mathfrak{t}}\mathcal{U}(\mathfrak{t},s)\mathscr{H}_1(s,\mathfrak{C}(s))ds-\frac{\mathfrak{r}^{\circledast}(1-\mathfrak{r})\mathfrak{t}^{\mathfrak{r}^{\circledast}-1}}{\mathcal{G}(\mathfrak{r})}\mathscr{H}_1(\mathfrak{t},\mathfrak{C}(\mathfrak{t}))\Bigg| \\
&\leq\mathscr{T}_1(\mathfrak{t}),\ \text{for all } \mathfrak{t}\in\mathcal{I}_{[0,T]}, \\
&\Bigg|\mathcal{N}(\mathfrak{t})-\frac{\mathfrak{r}\mathfrak{r}^{\circledast}}{\mathcal{G}(\mathfrak{r})\Gamma\mathfrak{r}}\int_0^{\mathfrak{t}}\mathcal{U}(\mathfrak{t},s)\mathscr{H}_2(s,\mathcal{N}(s))ds-\frac{\mathfrak{r}^{\circledast}(1-\mathfrak{r})\mathfrak{t}^{\mathfrak{r}^{\circledast}-1}}{\mathcal{G}(\mathfrak{r})}\mathscr{H}_2(\mathfrak{t},\mathcal{N}(\mathfrak{t}))\Bigg| \\
&\leq\mathscr{T}_2(\mathfrak{t}),\ \text{for all } \mathfrak{t}\in\mathcal{I}_{[0,T]}, \\
&\Bigg|\mathfrak{F}(\mathfrak{t})-\frac{\mathfrak{r}\mathfrak{r}^{\circledast}}{\mathcal{G}(\mathfrak{r})\Gamma\mathfrak{r}}\int_0^{\mathfrak{t}}\mathcal{U}(\mathfrak{t},s)\mathscr{H}_3(s,\mathfrak{F}(s))ds-\frac{\mathfrak{r}^{\circledast}(1-\mathfrak{r})\mathfrak{t}^{\mathfrak{r}^{\circledast}-1}}{\mathcal{G}(\mathfrak{r})}\mathscr{H}_3(\mathfrak{t},\mathfrak{F}(\mathfrak{t}))\Bigg| \\
&\leq\mathscr{T}_3(\mathfrak{t}),\ \text{for all } \mathfrak{t}\in\mathcal{I}_{[0,T]}, \\
&\Bigg|\mathfrak{T}(\mathfrak{t})-\frac{\mathfrak{r}\mathfrak{r}^{\circledast}}{\mathcal{G}(\mathfrak{r})\Gamma\mathfrak{r}}\int_0^{\mathfrak{t}}\mathcal{U}(\mathfrak{t},s)\mathscr{H}_4(s,\mathfrak{T}(s))ds-\frac{\mathfrak{r}^{\circledast}(1-\mathfrak{r})\mathfrak{t}^{\mathfrak{r}^{\circledast}-1}}{\mathcal{G}(\mathfrak{r})}\mathscr{H}_4(\mathfrak{t},\mathfrak{T}(\mathfrak{t}))\Bigg| \\
&\leq\mathscr{T}_4(\mathfrak{t}),\ \text{for all } \mathfrak{t}\in\mathcal{I}_{[0,T]}.
\end{aligned}
$$

There exists a solution $(\mathfrak{C}^{\circledast},\mathcal{N}^{\circledast},\mathfrak{F}^{\circledast},\mathfrak{T}^{\circledast})\in\mathscr{B}^4$ of the FF–$\mathscr{C}\mathscr{O}_2$ concentration dynamics (1.1), satisfying that

$$
\begin{aligned}
&|\mathfrak{C}(\mathfrak{t})-\mathfrak{C}^{\circledast}|\leq\delta_1\mathscr{T}_1(\mathfrak{t}),\ \text{for all } \mathfrak{t}\in\mathcal{I}_{[0,T]}, \\
&|\mathcal{N}(\mathfrak{t})-\mathcal{N}^{\circledast}|\leq\delta_2\mathscr{T}_2(\mathfrak{t}),\ \text{for all } \mathfrak{t}\in\mathcal{I}_{[0,T]}, \\
&|\mathfrak{F}(\mathfrak{t})-\mathfrak{F}^{\circledast}|\leq\delta_3\mathscr{T}_3(\mathfrak{t}),\ \text{for all } \mathfrak{t}\in\mathcal{I}_{[0,T]}, \qquad (2.7) \\
&|\mathfrak{T}(\mathfrak{t})-\mathfrak{T}^{\circledast}|\leq\delta_4\mathscr{T}_4(\mathfrak{t}),\ \text{for all } \mathfrak{t}\in\mathcal{I}_{[0,T]}.
\end{aligned}
$$

Theorem 2.6. *Under the consideration of hypothesis* $(\mathscr{H}^{\circledast})$*, the FF–*$\mathscr{C}\mathscr{O}_2$ *concentration dynamics* (1.1) *is HU-stable.*

Proof. We know that the FF–$\mathscr{C}\mathscr{O}_2$ concentration dynamics (1.1) has unique solution. Let there exists approximate solution of the model (1.1) $\mathfrak{C}^{\circledast}(\mathfrak{t})$, $\mathcal{N}^{\circledast}(\mathfrak{t})$, $\mathfrak{F}^{\circledast}(\mathfrak{t})$, $\mathfrak{T}^{\circledast}(\mathfrak{t})$, that satisfies the given model (1.1), such that

$$
\begin{aligned}
&|\mathfrak{C}(\mathfrak{t})-\mathfrak{C}^{\circledast}(\mathfrak{t})| \\
&=\Bigg|\Bigg(\frac{\mathfrak{r}\mathfrak{r}^{\circledast}}{\mathcal{G}(\mathfrak{r})\Gamma\mathfrak{r}}\int_0^{\mathfrak{t}}\mathcal{U}(\mathfrak{t},s)\mathscr{H}_1(s,\mathfrak{C}(s))ds+\frac{\mathfrak{r}^{\circledast}(1-\mathfrak{r})\mathfrak{t}^{\mathfrak{r}^{\circledast}-1}}{\mathcal{G}(\mathfrak{r})}\mathscr{H}_1(\mathfrak{t},\mathfrak{C}(\mathfrak{t}))\Bigg) \\
&-\Bigg(\frac{\mathfrak{r}\mathfrak{r}^{\circledast}}{\mathcal{G}(\mathfrak{r})\Gamma\mathfrak{r}}\int_0^{\mathfrak{t}}\mathcal{U}(\mathfrak{t},s)\mathscr{H}_1(s,\mathfrak{C}^{\circledast}(s))ds+\frac{\mathfrak{r}^{\circledast}(1-\mathfrak{r})\mathfrak{t}^{\mathfrak{r}^{\circledast}-1}}{\mathcal{G}(\mathfrak{r})}\mathscr{H}_1(\mathfrak{t},\mathfrak{C}^{\circledast}(\mathfrak{t}))\Bigg)\Bigg| \\
&=\frac{\mathfrak{r}\mathfrak{r}^{\circledast}}{\mathcal{G}(\mathfrak{r})\Gamma\mathfrak{r}}\int_0^{\mathfrak{t}}\mathcal{U}(\mathfrak{t},s)|\mathscr{H}_1(s,\mathfrak{C}(s)-\mathscr{H}_1(s,\mathfrak{C}^{\circledast}(s))|ds \\
&+\frac{\mathfrak{r}^{\circledast}(1-\mathfrak{r})\mathfrak{t}^{\mathfrak{r}^{\circledast}-1}}{\mathcal{G}(\mathfrak{r})}|\mathscr{H}_1(\mathfrak{t},\mathfrak{C}(\mathfrak{t})-\mathscr{H}_1(\mathfrak{t},\mathfrak{C}^{\circledast}(\mathfrak{t}))| \\
&\leq\Bigg(\frac{\mathfrak{r}\mathfrak{r}^{\circledast}}{\mathcal{G}(\mathfrak{r})\Gamma\mathfrak{r}}\int_0^{\mathfrak{t}}\mathcal{U}(\mathfrak{t},s)+\frac{\mathfrak{r}^{\circledast}(1-\mathfrak{r})\mathfrak{t}^{\mathfrak{r}^{\circledast}-1}}{\mathcal{G}(\mathfrak{r})}\Bigg)\phi_1\|\mathfrak{C}-\mathfrak{C}^{\circledast}\|
\end{aligned}
$$

$$\leq \left(\frac{\mathfrak{r}\mathfrak{r}^{\circledast}\Gamma\mathfrak{r}^{\circledast}}{\mathscr{G}(\mathfrak{r})\Gamma(\mathfrak{r}+\mathfrak{r}^{\circledast}))} + \frac{\mathfrak{r}^{\circledast}(1-\mathfrak{r})}{\mathscr{G}(\mathfrak{r})} \right) \phi_1 \|\mathfrak{C} - \mathfrak{C}^{\circledast}\|$$

Let $\alpha_1 = \left(\frac{\mathfrak{r}\mathfrak{r}^{\circledast}\Gamma\mathfrak{r}^{\circledast}}{\mathscr{G}(\mathfrak{r})\Gamma(\mathfrak{r}+\mathfrak{r}^{\circledast}))} + \frac{\mathfrak{r}^{\circledast}(1-\mathfrak{r})}{\mathscr{G}(\mathfrak{r})} \right) \|\mathfrak{C} - \mathfrak{C}^{\circledast}\|$, $\zeta_1 = \phi_1$, so the above inequality becomes $|\mathfrak{C} - \mathfrak{C}^{\circledast}| \leq \delta_1\zeta_1$. Similarly, by the consideration of hypothesis $(\mathscr{K}^{\circledast})$, we get $|\mathfrak{C} - \mathfrak{C}^{\circledast}| \leq \delta_2\zeta_2$, where $\zeta_2 = \phi_2$. Also, for the $\mathfrak{F}$ and $\mathfrak{T}$, we have $|\mathfrak{F} - \mathfrak{F}^{\circledast}| \leq \delta_3\zeta_3$, where $\zeta_3 = \phi_3$ and $|\mathfrak{T} - \mathfrak{T}^{\circledast}| \leq \delta_4\zeta_4$, where $\zeta_4 = \phi_4$. Consequently, the FF–$\mathscr{CO}_2$ concentration dynamics (1.1) is HU-stable. □

Theorem 2.7. *With assumption $(\mathscr{K}^{\circledast})$, the FF–$\mathscr{CO}_2$ concentration dynamics (1.1) is generalized HUR-stable.*

Proof. The proof of this Theorem can be obtained with the same work given in the proof of the Theorem 2.6 with the addition of Definition 2.5. □

3. Numerical scheme

The numerical scheme for FF–$\mathscr{CO}_2$ concentration dynamics (1.1) is provided in this portion of the paper.

Let us consider ${}^{FFM}{}_0D_{\mathfrak{t}}^{\varsigma_1,\varsigma_2}\mathscr{E}(\mathfrak{t}) = \Omega(\mathfrak{t}, \mathscr{E}(\mathfrak{t}))R$ where $\mathscr{E}(0) = \mathscr{E}_0$ The above equation can be written in Antangana Baleanu FF derivative as follows:

$${}^{FFR}{}_0D_{\mathfrak{t}}^{\varsigma_1}\mathscr{E}(\mathfrak{t}) = \varsigma_2 t^{\varsigma_2-1}\mathcal{L}(\mathfrak{t}, \mathscr{E}(\mathfrak{t})) = \Omega(\mathfrak{t}, \mathscr{E}(\mathfrak{t})) \tag{3.1}$$

Taking Antangana Baleanu integral, we get

$$\mathscr{E}(\mathfrak{t}) = \mathscr{E}(0) + \frac{1-\varsigma_1}{\mathscr{G}(\varsigma_1)}\Omega(\mathfrak{t}, \mathscr{E}(\mathfrak{t})) + \frac{\varsigma_1}{\mathscr{G}(\varsigma_1)\Gamma\varsigma_1}\int_0^{\mathfrak{t}} \zeta^{\varsigma_2-1}(\mathfrak{t}-\zeta)^{\varsigma_1-1}\Omega(\zeta, \mathscr{E}(\zeta))d\zeta \tag{3.2}$$

Replacing $(\mathfrak{t})$ by t_{n+1} we have

$$\mathscr{E}^{n+1} = \mathscr{E}(0) + \frac{1-\varsigma_1}{\mathscr{G}(\varsigma_1)}\Omega(\mathfrak{t}_n, \mathscr{E}(\mathfrak{t}_n)) + \frac{\varsigma_1}{\mathscr{G}(\varsigma_1)\Gamma\varsigma_1}\int_0^{\mathfrak{t}^{n+1}} \zeta^{\varsigma_2-1}(\mathfrak{t}_{n+1}-\zeta)^{\varsigma_1-1}\Omega(\zeta, \mathscr{E}(\zeta))d\zeta \tag{3.3}$$

By Lagrange Polynomial (LP) of two steps, we have

$$\begin{aligned}\Omega(u, \mathscr{E}(u)) &\approx \frac{(u-t_{k-1})\Omega(\mathfrak{t}_k, \mathscr{E}_{\mathfrak{t}_k})}{t_k - t_{k-1}} - \frac{(u-t_k)\Omega(\mathfrak{t}_{k-1}, \mathscr{E}_{\mathfrak{t}_{k-1}})}{t_k - t_{k-1}} \\ &= \frac{\Omega(\mathfrak{t}_k, \mathscr{E}_{\mathfrak{t}_k})(u-t_{k-1})}{t_k - t_{k-1}} - \frac{\Omega(\mathfrak{t}_{k-1}, \mathscr{E}_{\mathfrak{t}_{k-1}})(u-t_k)}{t_k - t_{k-1}} \\ &= \frac{\Omega(\mathfrak{t}_k, \mathscr{E}_k)(u-t_{k-1})}{h} - \frac{\Omega(\mathfrak{t}_{k-1}, \mathscr{E}_{k-1})(u-t_k)}{h}\end{aligned} \tag{3.4}$$

Applying LP to (3.3), we get

$$\begin{aligned}\mathscr{E}^{n+1} &= \mathscr{E}(0) + \frac{1-\varsigma_1}{\mathscr{G}(\varsigma_1)}\Omega(\mathfrak{t}_n, \mathscr{E}(\mathfrak{t}_n)) \\ &+ \frac{\varsigma_1}{\mathscr{G}(\varsigma_1)\Gamma\theta_1}\sum_{i=1}^{n}\left[\frac{\Omega(\mathfrak{t}_i, \mathscr{E}(\mathfrak{t}_i))}{h}\int_{t_k}^{\mathfrak{t}^{k+1}}(\zeta - t_{i-1})(\mathfrak{t}_{n+1}-\zeta)^{\varsigma_1-1}d\zeta\right. \\ &\left. - \frac{\Omega(\mathfrak{t}_{i-1}, \mathscr{E}(\mathfrak{t}_{i-1}))}{h}\int_{t_k}^{\mathfrak{t}^{n+1}}(\zeta - t_i)(\mathfrak{t}_{n+1}-\zeta)^{\varsigma_1-1}d\zeta\right]\end{aligned} \tag{3.5}$$

Now solving the integral we get

$$\begin{aligned}\mathscr{E}^{n+1} &= \mathscr{E}(0) + \frac{1-\varsigma_1}{\mathscr{G}(\varsigma_1)}\Omega(\mathfrak{t}_n, \mathscr{E}(\mathfrak{t}_n)) \\ &+ \frac{\varsigma_1 h^{\varsigma_1}}{\Gamma(\varsigma_1+2)}\sum_{i=1}^{n}\left[\Omega(\mathfrak{t}_i, \mathscr{E}(\mathfrak{t}_i))\left((n+1-i)^{\varsigma_1}(n-i+2+\varsigma_1)\right.\right. \\ &\left. - (n-i)^{\varsigma_1}(n-i+2+2\varsigma_1)\right) \\ &\left. - \Omega(\mathfrak{t}_{i-1}, \mathscr{E}_{i-1})\left((n+1-i)^{\varsigma_1+1} - (n-i+1+\varsigma_1)(n-i)^{\varsigma_1}\right)\right]\end{aligned} \tag{3.6}$$

Applying this numerical scheme (3.6) to the FF–$\mathscr{CO}_2$ concentration dynamics (1.1), we get numerical data given in Fig. 4. In Fig. 4, there are four subfigures. The $\mathscr{CO}_2$ concentration is presented in subFig. 4a which shows that the $\mathscr{CO}_2$ concentration is getting higher with respect to the time t. This increase is due to the reduction of the forest area $\mathfrak{F}$ and increase in the human population $\mathcal{N}$ by deforestation which are given for different fractional orders in the subFig. 4c and subFig. 4d. It is expected that if there were no new plantation efforts then the $\mathscr{CO}_2$ concentration in the atmosphere would further increase. The decreased population is transferred into the SubFig. 4b and 4c. For the computational results, we have used the numerical values: $\Omega = 1.68$, $\lambda = 0.564$, $\alpha = 0.006; \lambda_1 = 7.5681 \times 10^{-7}$, $r = 0.026$, $K = 11; \theta = 5.3765 \times 10^{-8}$, $u = 0.005$, $M = 5900$, $\phi = 0.00042371$, $\pi_1 = 0.005$, $\gamma_1 = 5 \times 10^{-7}$, $K_1 = 300$, $\beta = 3 \times 10^{-6}$, $\upsilon = 0.004$, $\nu_0 = 0.01$.

4. Applications of AI and NN-tools

Artificial intelligence (AI) and neural networking are revolutionizing research in the field of dynamical systems offering sophisticated techniques for modeling and interpretation. Neural networks, which are a part of artificial intelligence, are highly effective at working with the complexity of dynamic systems. They attain this by analyzing enormous datasets, learning patterns, and calculating nonlinear functions that represent the state of the system. Artificial Intelligence (AI) and neural network tools utilize advanced mathematical and statistical techniques to analyze complex data and uncover patterns. The feedforward process in neural networks is mathematically represented as:

$$\mathbf{y} = f\left(\mathbf{W}_L \cdot \sigma\left(\mathbf{W}_{L-1} \cdot \cdots \cdot \sigma\left(\mathbf{W}_1 \cdot \mathbf{x} + \mathbf{b}_1\right) + \mathbf{b}_{L-1}\right) + \mathbf{b}_L\right)$$

where $\mathbf{x}$ is the input vector, $\mathbf{W}_i$ are weight matrices, $\mathbf{b}_i$ are bias vectors, $\sigma(\cdot)$ denotes activation functions such as ReLU, sigmoid, or tanh, and $f(\cdot)$ is the output function. For model training, various loss functions are employed to quantify prediction errors. Common loss functions include: **Mean Squared Error (MSE)** for regression:

$$\mathcal{L}(\mathbf{y}, \hat{\mathbf{y}}) = \frac{1}{N}\sum_{i=1}^{N}(\hat{y}_i - y_i)^2$$

and **Cross-Entropy Loss** for classification:

$$\mathcal{L}(\mathbf{y}, \hat{\mathbf{y}}) = -\sum_{i=1}^{C} y_i \log(\hat{y}_i)$$

where $\hat{\mathbf{y}}$ represents predicted values, $\mathbf{y}$ denotes actual values, N is the number of samples, and C is the number of classes. Optimization of the network parameters is typically done using gradient-based methods such as Stochastic Gradient Descent (SGD):

$$\mathbf{W}_{new} = \mathbf{W}_{old} - \eta\nabla_{\mathbf{W}}\mathcal{L}$$

where η is the learning rate and $\nabla_{\mathbf{W}}\mathcal{L}$ is the gradient of the loss function with respect to the weights. To enhance model performance and generalization, techniques like Batch Normalization and Dropout are also applied. Batch Normalization normalizes the input of each layer:

$$\hat{x}_i = \frac{x_i - \mu}{\sigma} \cdot \gamma + \beta$$

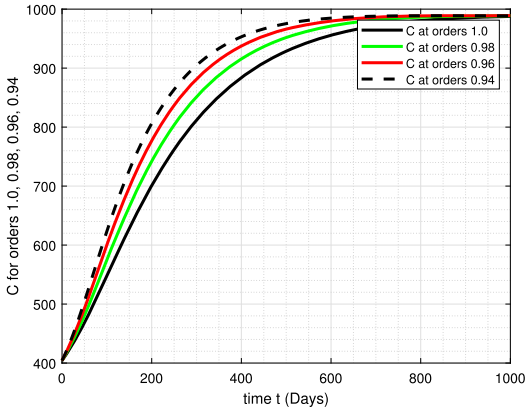

(a) Computational results for the concentration of the $\mathscr{CO}_2$ for different FF-orders.

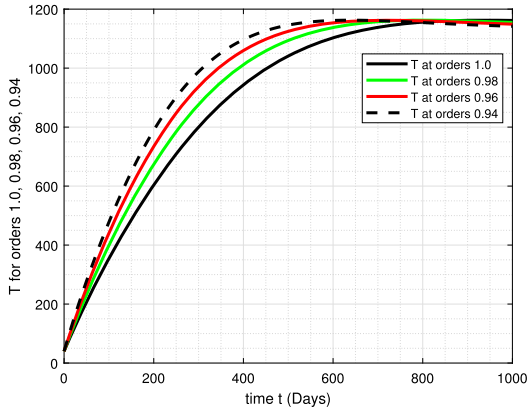

(b) Computational results for the Plantation efforts Υ for different FF-orders.

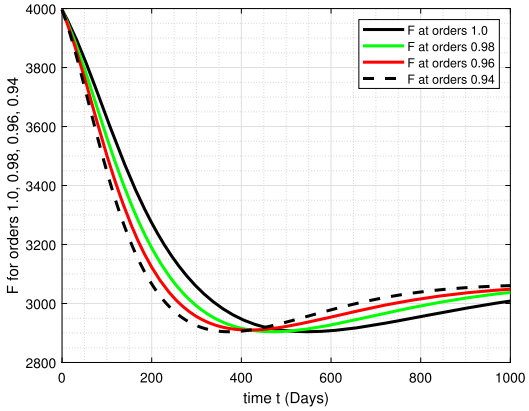

(c) Computational results for the forest area $\digamma$ for different FF-orders.

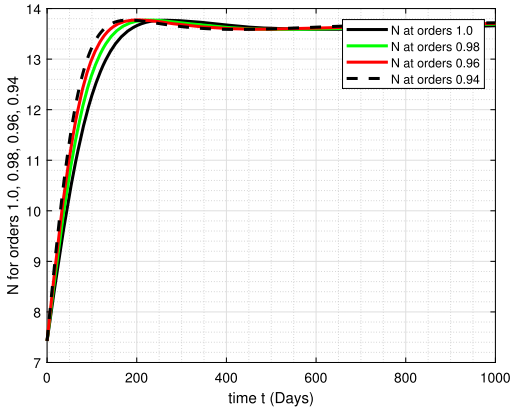

(d) Computational results for the human population in the area $\mathcal{N}$ for different FF-orders.

Fig. 4. The computational plots for the dynamics of the FF-$\mathscr{CO}_2$ model (1.1).

where μ and σ are the mean and standard deviation of the batch, and γ and β are learned parameters. Dropout randomly deactivates neurons during training to prevent overfitting. Neural networks has the capability of expressing systems using empirical data, leading accurate predictions of future, without relying on explicit equations utilized by previous techniques with fast computing is shown in the Fig. 6. This skill is especially useful for sciences like epidemiology, where it is possible to predict the spread of illnesses by looking at historical data. Also, neural networks enhance control systems, therefore improving the effectiveness of activities across various domains, such as engineering and environmental management. Reinforcement methods for learning extend the significance of AI by actively searching for optimal control mechanisms in real-time, consequently strengthening the study and practical application of dynamical systems. The integration of AI and neural networking with computationally complex systems not only improves understanding but also motivates novel methodologies, boosting the capabilities of mathematical modeling and estimation.

In this section, we employ artificial intelligence (AI) and neural networks (NN) to computationally analyze the dynamics of FF–$\mathscr{CO}_2$ value according to (1.1). We also evaluate the effectiveness of the numerical approach that was investigated for the model in section 3. The depiction is presented with numerous computational figures.

Fig. 5 illustrates the comprehensive analysis of FF–$\mathscr{CO}_2$ concentration dynamics described in (1.1).

- **SubFig. 5a**: Describes the steps used to train and test the $\mathscr{CO}_2$ concentration data at epochs 303, with a gradient value of 0.079855 and a value of $\mu = 0.0001$. There are also 6 validation checks. It is shown that the model can predict $\mathscr{CO}_2$ concentration. This shows that there is a strong link between the training dataset and the model's output, which proves the model's dependability.
- **SubFig. 5b**: Displays a histogram with 20 bins, illustrating the difference between planned and target values of $\mathscr{CO}_2$ concentration. This histogram shows the variance and magnitude of differences between the actual and projected values, allowing for an assessment of the accuracy and dependability of the algorithm.
- **SubFig. 5c**: Demonstrates its precision of the algorithm employed in analyzing the data of $\mathscr{CO}_2$ concentration with epoch 297 with best validation 0.00039678. This part of the figure shows that the method works to show the data correctly and capture the complicated changes in the FF–$\mathscr{CO}_2$ concentration changes that are shown in (1.1).
- **SubFig. 5d**: Demonstrates the fitting of data and giving the joint outputs for Training data, output data, validation targets, validation outputs, test outputs and targets, errors and fit data. All these results are in good agreement with each other and showing a smaller error in the algorithm for the comparative targets and outputs, for the FF–$\mathscr{CO}_2$ concentration measured by the model (1.1).

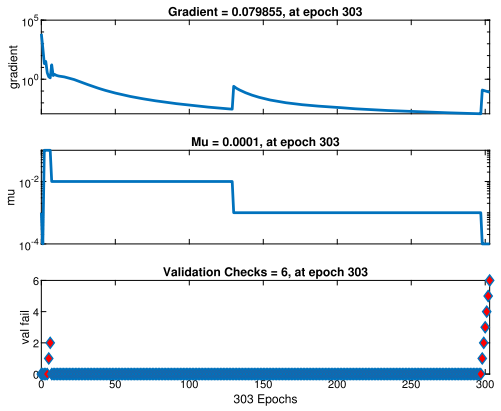

(a) Training data of the $\mathscr{CO}_2$ of (1.1).

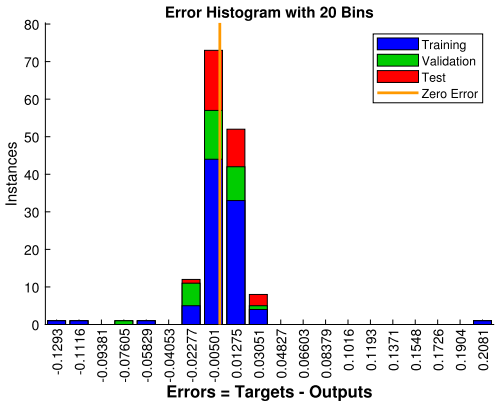

(b) Error histogram for the Carbon dioxide data of the model (1.1).

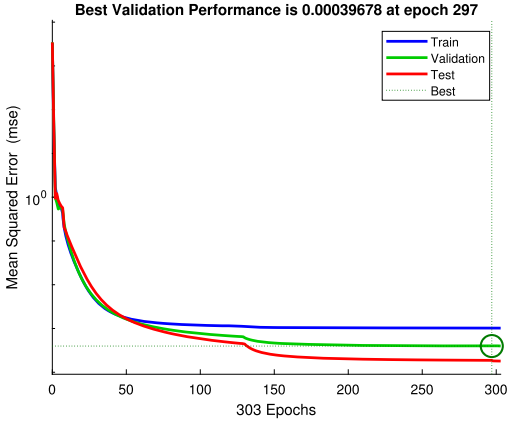

(c) Performance of the computational technique evaluated by the AI and NN tools forthe $\mathscr{CO}_2$ of the model (1.1).

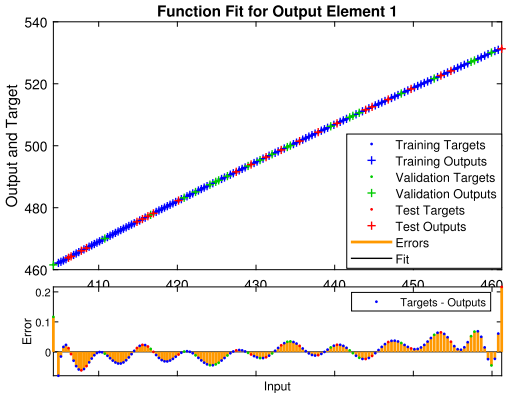

(d) Fitting data for the $\mathscr{CO}_2$ of the model (1.1).

Fig. 5. AI approach for the data analysis of the $\mathscr{CO}_2$ of the model (1.1).

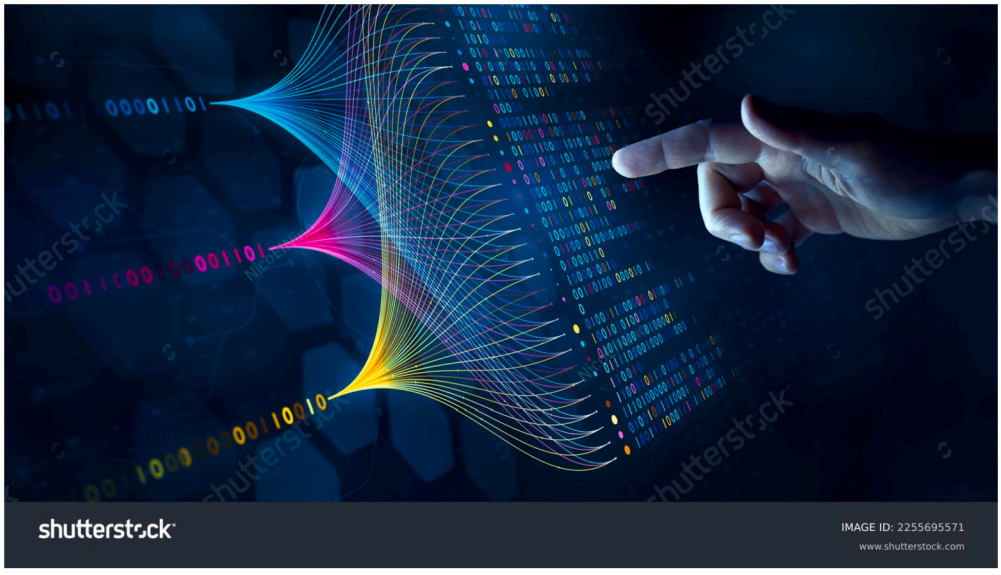

Fig. 6. Artificial neural networking for data analysis with fast computing [43].

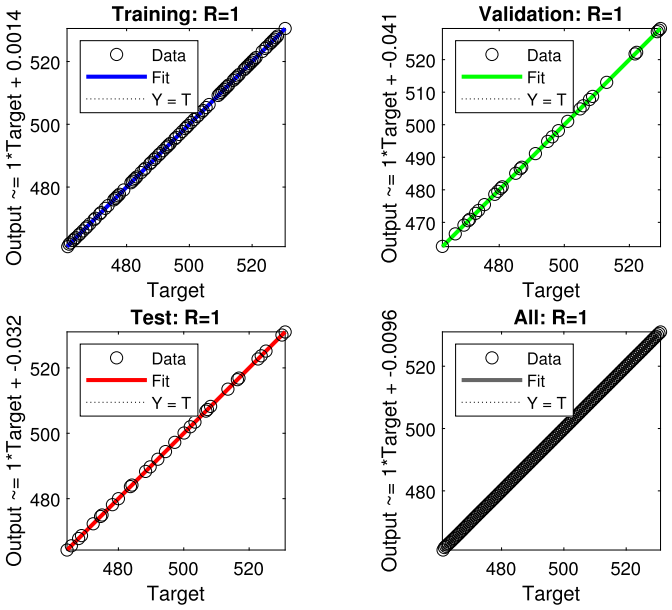

Fig. 7. Regression for the data for $\mathscr{C}\mathscr{O}_2$ concentration with the use of AI.

Overall, the results show that the model can help us understand how the concentration of FF–$\mathscr{C}\mathscr{O}_2$ changes over time, as shown in equation (1.1). The use of AI and neural networking in this study is important because it improves the models' accuracy and reliability and can give a good comparative analysis of the targeted values and the input values of the model's simulations.

Fig. 7 illustrates the regression analysis carried out on the relationship between FF–$\mathscr{C}\mathscr{O}_2$ concentration dynamics, outlined in (1.1), utilizing advanced computational techniques. A correlation value (R) of 1 implies a perfect agreement between expected and input $\mathscr{C}\mathscr{O}_2$ concentration dynamics, reflecting high precision in the simulations. The significant level of accuracy that was shown in this analysis underscores the advantages of algorithms for figuring out and forecasting the dynamics of the FF–$\mathscr{C}\mathscr{O}_2$ concentration dynamics (1.1).

Fig. 7 shows the findings of regression analysis for the dynamics of FF–$\mathscr{C}\mathscr{O}_2$ concentration, outlined in equation (1.1), utilizing AI and neural networking techniques. In this study, we examined a dataset consisting of 300 values. This dataset had 150 predictors and 150 answers. The chosen algorithm was Random data division, with the Levenberg-Marquardt training algorithm. The performance was evaluated using AI tools by analyzing the mean squared error. The observations were divided into three categories: Training (104), Validation (23), and Test (23). The mean squared errors (MSE) for these values were derived as follows: 6.2987×10^{-14}, 2.5836×10^{-11}, and 5.1648×10^{-12}, respectively. Fig. 8 illustrates the auto correlation and hits results obtained using Neural networking clustering for $\mathscr{C}\mathscr{O}_2$ concentration dynamics given (1.1). It is based on two sugfigures. The subFig. 8a displays the autocorrelation of data of $\mathscr{C}\mathscr{O}_2$ concentration dynamics given (1.1). This analysis helps in understanding the persistence and periodicity of FF–$\mathscr{C}\mathscr{O}_2$ concentration dynamics (1.1). While, the subFig. 8b illustrates the simple hits of data of $\mathscr{C}\mathscr{O}_2$ concentration dynamics given (1.1), demonstrating clusters within the dataset that correlate with the model's predictions. This visual representation aids in identifying patterns and validating the model's forecasting accuracy.

Fig. 9 illustrates the results accomplished through NN clustering for FF–$\mathscr{C}\mathscr{O}_2$ concentration dynamics of (1.1). The illustration is derived from two subdiagrams. Fig. 9a displays the clustering of weight planes in $\mathscr{C}\mathscr{O}_2$ concentration dynamics of (1.1), demonstrating the presence of various groups characterized by different underlying properties. This study facilitates recognizing of changes in $\mathscr{C}\mathscr{O}_2$ concentration and possible components that affect the dynamics of the concentration. Fig. 9b shows the clustering of weight places of $\mathscr{C}\mathscr{O}_2$ concentration data using the NN algorithm. It specifically highlights the clusters that are in line with the assumptions made by the FF–$\mathscr{C}\mathscr{O}_2$ concentration dynamics (1.1). This illustration enables to confirm the preciseness of the model and advance in insight into the intricate relationships within the dynamics of FF–$\mathscr{C}\mathscr{O}_2$ concentration, which is explained by equation (1.1).

4.1. Nonlinear time series data analysis

For the Carbon dioxide analysis of the model (1.1), we have considered time series data analysis with 150 input data and 150 target data. The data division was considered as random using Levenberg-Marquardt algorithm to perform mean square error while keeping layer size 10 and time delay 2. We have recorded for the training data of 104 observations, $MSE = 4.2239\times10^{-14}$ and $R = 1$. For the validation with 22 observations, we have analyzed $MSE = 5.7409\times10^{-14}$ and $R = 1$ and for the test 22 observations resulted $MSE = 2.0654\times10^{-13}$ and $R = 1$.

In this section, we apply the AI and NN for the computational analysis of the $\mathscr{C}\mathscr{O}_2$ concentration dynamics (1.1) and analyse the capabilities of the numerical scheme that was studied for the model in the section 3. This illustration is given in several computational figures.

Description of Fig. 10 and 11 illustrate the comprehensive analysis of $\mathscr{C}\mathscr{O}_2$ concentration dynamics described in (1.1) and were obtained with the NLTSP AI tool NARX.

- **SubFig. 10a**: Presents the validation and training process for the infected human population of time series data at 1000 epoch with gradient 5.7782×10^{-06}, $\mu = 0.1$ and val fail 0. It shows the model's ability to accurately predict $\mathscr{C}\mathscr{O}_2$ concentration dynamics described in (1.1).
- **SubFig. 10b**: Providing the error histogram with 20 bins based on training, validation, test and zero error data. The concentrations of the graphs are surrounded by the zerro error for the data of $\mathscr{C}\mathscr{O}_2$ concentration dynamics described in (1.1)
- **SubFig. 10c**: Identifies the accuracy of the computational method employed to analyze the output and target for the time series data of $\mathscr{C}\mathscr{O}_2$ concentration dynamics described in (1.1). This subfigure shows the efficacy of the algorithm in precisely representing the computational data and capturing the intricate dynamics of $\mathscr{C}\mathscr{O}_2$ concentration dynamics as defined by equation (1.1). This subgraph is a joint representation of the data for the training targets, training outputs, validation of targets, validation of outputs, test targets and test targets, errors and response data.
- **SubFig. 10d**: is describing the response of output data with a very small error of 20×10^{-7}.
- **SubFig. 11a**: is presenting the autocorrelation error in the input and target data. This graph is a computational data obtained by the NN-Tool NARX for the $\mathscr{C}\mathscr{O}_2$ data with an error of less than 7×10^{-14}.
- **SubFig. 11b:** is presenting correlation between input and error which is obtain by computing the corresponding differences of targets and inputs data. This graph is a computational data obtained by the NN-Tool NARX for the $\mathscr{C}\mathscr{O}_2$ concentration analysis.

The results strongly support the model's ability to give useful information about the dynamics of $\mathscr{C}\mathscr{O}_2$ concentration as shown in (1.1). Using AI and neural networks in this study is very important because it improves the accuracy and dependability of the estimations. This leads to more accurate public health measures and methods to optimize the $\mathscr{C}\mathscr{O}_2$ concentration dynamics, as shown in (1.1).

5. Conclusion

This article provide a comprehensive analysis of atmospheric $\mathscr{C}\mathscr{O}_2$ concentration dynamics (1.1) through theoretical as well as computational techniques. The findings are summarized in the description as well in the pie chart Fig. 12.

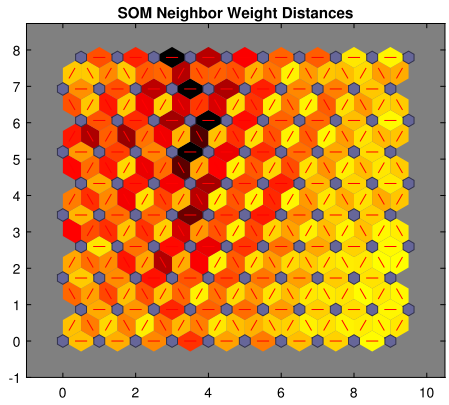

(a) Autocorrelation of $\mathscr{CO}_2$.

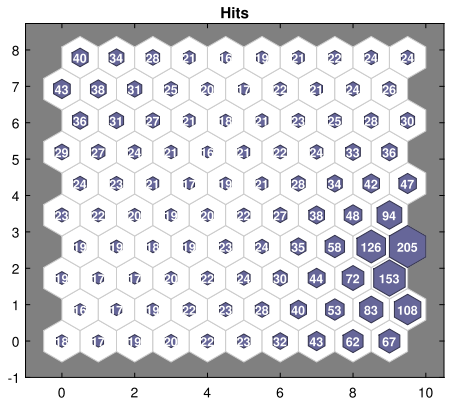

(b) NN-clustering for simple hits of $\mathscr{CO}_2$ data.

Fig. 8. NN-clustering for the analysis of autocorrelation and simple hits for $\mathcal{N}$ data.

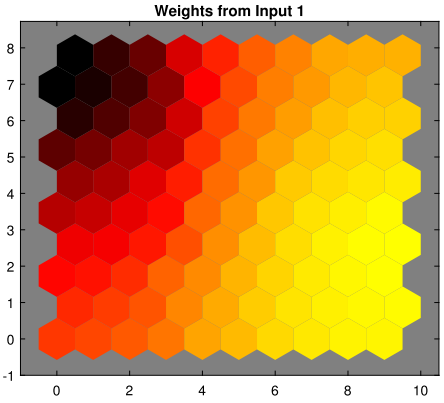

(a) NN-clustering for weight planes of $\mathscr{CO}_2$ concentration.

(b) NN-Clustering for weight positions of $\mathscr{CO}_2$ data.

Fig. 9. NN-clustering for the weight planes and weight positions of $\mathscr{CO}_2$ data.

- In this study of $\mathscr{CO}_2$ concentration dynamics (1.1), we conducted a deep analysis encompassing theoretical and computational investigations.
- Section 1 is on the theoretical exploration, establishing important aspects of the $\mathscr{CO}_2$ concentration dynamics (1.1) including the existence and uniqueness of solutions, as well as Hyers-Ulam stability. These results provide a foundational understanding of the model's dynamics and robustness in predicting $\mathscr{CO}_2$ concentration as per our presumed model (1.1).
- Section 2 involves a computational approach with the implementation of a numerical scheme to simulate the $\mathscr{CO}_2$ concentration dynamics (1.1). This enabled detailed data generation across subclasses, analyzed using AI and neural networking techniques.
- Computational results are illustrated in several figures. Applying the numerical scheme (3.6) to the FF–$\mathscr{CO}_2$ concentration dynamics (1.1), we get the numerical data given in Fig. 4. In Fig. 4, there are four subfigures. The dynamics of the $\mathscr{CO}_2$ level is presented in subFig. 4a which shows growth in concentration with respect to the time t. This increase is due to the reduction of the forest area $\mathfrak{F}$ and the increase in the human population $\mathcal{N}$ by deforestation, which are given for different fractional orders in the subFig. 4c and subFig. 4d. It is expected that if there were no new plantation efforts and control strategies then the $\mathscr{CO}_2$ concentration in the atmosphere would further increase and will affect the ecosystem of the planet more severely than shown in the Fig. 3. These results are then analysed with the help of AI and NN tools.
- Further analysis in Figs. 5, 7, 8, and 9 highlights the exceptional accuracy and robustness of our computational methods, demonstrating high correlation coefficients and effective clustering analyses. These results underscore the efficacy of computational modeling in predicting disease transmission patterns, informing targeted public health interventions.
- Fig. 10 and Fig. 11 are describing time series data analysis using the NARX tool with 70% training data, 15% test data and 15% validation data with layer size 10.
- The findings of the article are statistically summarized in the piechart diagram Fig. 12.
- Our integrated theoretical and computational approach not only advances understanding of $\mathscr{CO}_2$ dynamics (1.1) but also emphasizes the importance of advanced computational tools in disease modeling.
- This study provides valuable insights for future research and proactive measures to combat $\mathscr{CO}_2$ concentration (1.1) globally.

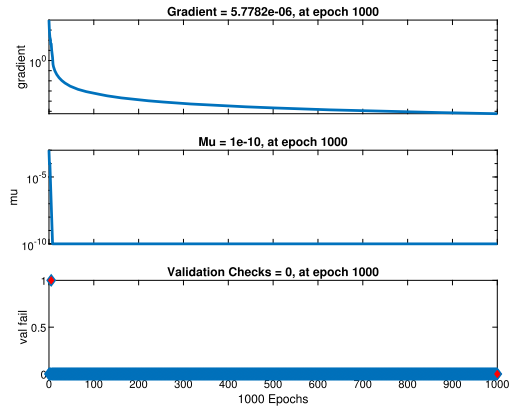

(a) Training data by the NLTSP using NARX networking for the $\mathcal{N}$ of $\mathscr{CO}_2$ concentration dynamics in (1.1).

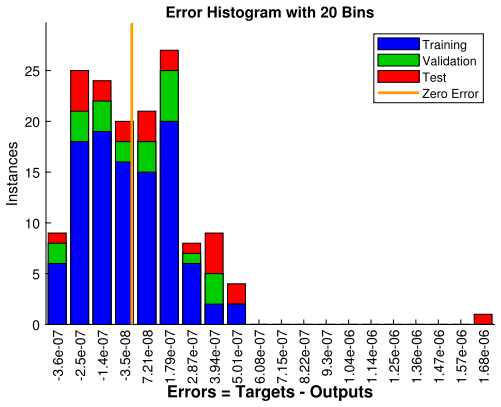

(b) Error histogram by the NLTSP using NARX networking for the $\mathcal{N}$ of the $\mathscr{CO}_2$ concentration dynamics (1.1).

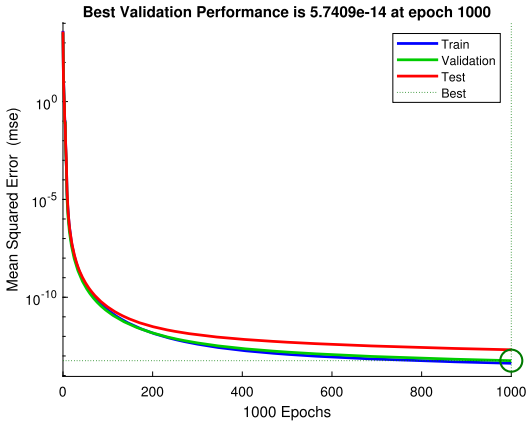

(c) Performance analysis of the computations by the NLTSP using NARX networking for the $\mathscr{CO}_2$ concentration measured by the FF-$\mathscr{CO}_2$ model (1.1).

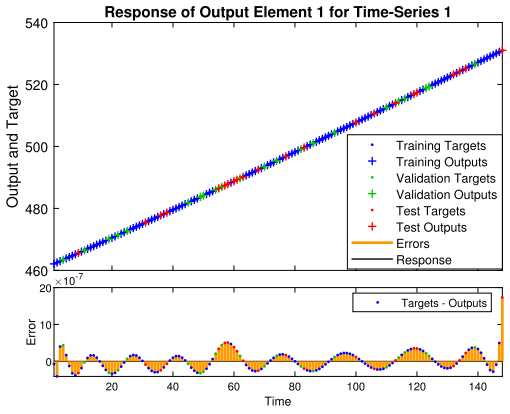

(d) Response analysis by the NLTSP using NARX networking for the $\mathcal{N}$ of the $\mathscr{CO}_2$ concentration dynamics in (1.1).

Fig. 10. Time series data analysis of the $\mathscr{CO}_2$ concentration dynamics (1.1) by the use of NARX tool of AI.

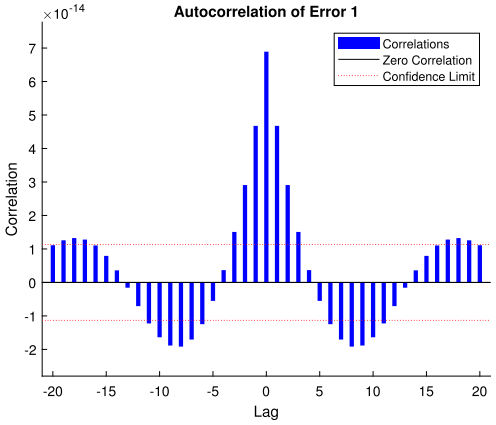

(a) Computational results for error correlation by NN-Tool NARX for $\mathscr{CO}_2$.

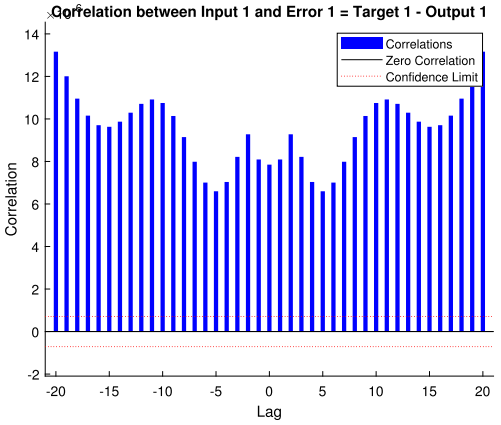

(b) Computational results for input error correlation by NN-Tool NARX for $\mathscr{CO}_2$.

Fig. 11. Time series data analysis of the FF-$\mathscr{CO}_2$ concentration dynamics (1.1) by the use of NARX tool of AI.

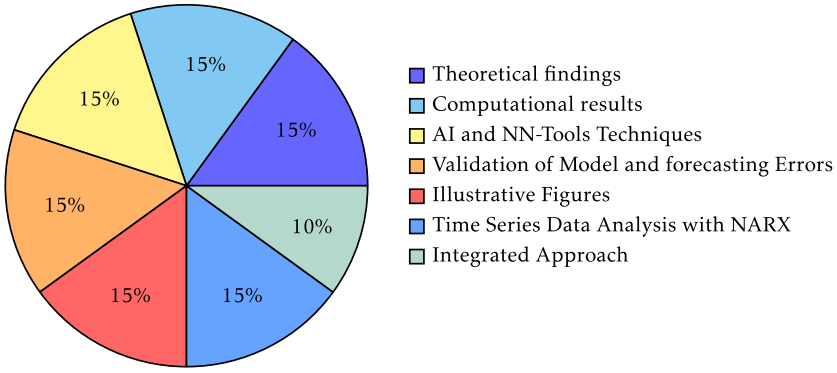

Fig. 12. Pie chart summary of the work analyzing the $\mathscr{CO}_2$ concentration based on the AI and NN-Tools.

Future Directions:

- To generalize the FF model to incorporate environmental and age factors influencing $\mathscr{CO}_2$ concentration dynamics (1.1) in a population.
- To analyze real-time data from different regions to improve the model's robustness and predictive precision.
- To investigate the role of interventions such as vaccination strategies or vector control measures within the FF framework to highlight effective public health measures against $\mathscr{CO}_2$ concentration dynamics.

CRediT authorship contribution statement

Hasib Khan: Validation, Software, Investigation. **Mahmoud Abdel-Aty:** Software, Investigation, Formal analysis. **D.K. Almutairi:** Software, Investigation, Formal analysis. **J.F. Gómez-Aguilar:** Software, Investigation, Formal analysis. **Jehad Alzabut:** Validation, Software, Investigation.

Compliance with Ethics requirements

This article fulfill all the ethical requirements of publication in any journal. The simulation data is our own which was derived by the computational technique explained in the paper while any relevant material is well cited in the paper. Also, there is no conflict of the authors.

Declaration of competing interest

The authors declare that there is no conflict of interest regarding the publication of this paper.

Acknowledgements

H. Khan and J. Alzabut are thankful to Prince Sultan University for their financial support to the research work and publication in the journal. J. Alzabut also thanks the OSTIM Technical University for his help. D. K. Almutairi extends her appreciation to the Deanship of Postgraduate Studies and Scientific Research at Majmaah University for funding this research work.

Data availability

Data sharing not applicable to this article as no data-sets were generated or analyzed during the current study.

References

[1] Gammon RH, Sundquist ET, Fraser PJ. History of carbon dioxide in the atmosphere. In: Atmospheric carbon dioxide and the global carbon cycle; 1985. p. 25–62.
[2] Alvarez R, Carmona E, Marin JM, Poveda ML, Gutierrez-Puebla E, Monge A. Carbon dioxide chemistry. Synthesis, properties, and structural characterization of stable bis (carbon dioxide) adducts of molybdenum. J Am Chem Soc 1986;108(9):2286–94.
[3] Vitousek PM. Beyond global warming: ecology and global change. Ecology 1994;75(7):1861–76.
[4] Cox PM, Betts RA, Jones CD, Spall SA, Totterdell IJ. Acceleration of global warming due to carbon-cycle feedbacks in a coupled climate model. Nature 2000;408(6809):184–7.
[5] Friedlingstein P, O'sullivan M, Jones MW, Andrew RM, Gregor L, Hauck J, et al. Global carbon budget 2022. Earth Syst Sci Data 2022;14(11):4811–900.
[6] Zheng Y, Ou J, Chen G, Wu X, Liu X. Mapping building-based spatiotemporal distributions of carbon dioxide emission: a case study in England. Int J Environ Res Public Health 2022;19(10):5986.
[7] Deng Z, Ciais P, Hu L, Martinez A, Saunois M, Thompson RL, et al. Global Greenhouse gas reconciliation 2022. Earth Syst Sci Data Discuss 2024:1–47.
[8] Xu Z, Liu L, Wu L. Forecasting the carbon dioxide emissions in 53 countries and regions using a non-equigap grey model. Environ Sci Pollut Res 2021;28:15659–72.
[9] Samour A, Moyo D, Tursoy T. Renewable energy, banking sector development, and carbon dioxide emissions nexus: a path toward sustainable development in South Africa. Renew Energy 2022;193:1032–40.
[10] Liu Z, Chen C, Wang G, Li S, Liu S. Regional sea level response to external forcings from the twentieth to the twenty-first century. J Clim 2024;37(11):3237–48.
[11] Song J, Tong G, Chao J, Chung J, Zhang M, Lin W, et al. Data driven pathway analysis and forecast of global warming and sea level rise. Sci Rep 2023;13(1):5536.
[12] Boumis G, Moftakhari HR, Moradkhani H. Coevolution of extreme sea levels and sea-level rise under global warming. Earths Future 2023;11(7):1–10.
[13] Smith MR, Myers SS. Impact of anthropogenic CO2 emissions on global human nutrition. Nat Clim Change 2018;8(9):834–9.
[14] Filippini T, Paduano S, Veneri F, Barbolini G, Fiore G, Vinceti M. Adverse human health effects of climate change: an update. Ann Igiene 2024;36(3):281–91.
[15] Friedman D. Toxicity of carbon dioxide gas exposure, CO2 poisoning symptoms, carbon dioxide exposure limits, and links to toxic gas testing procedures. InspectAPedia. http://www.inspectapedia.com/hazmat/CO2gashaz.htm. [Accessed 15 July 2015].
[16] Farkas M. Dynamical models in biology. Academic Press; 2001 Jun 15.
[17] Gudala M, Tariq Z, Govindarajan SK, Yan B, Sun S. Fractured geothermal reservoir using CO2 as geofluid: numerical analysis and machine learning modeling. ACS Omega 2024;9(7):7746–69.
[18] Zhao S, Chen H. Modeling the epidemic dynamics and control of COVID-19 outbreak in China. Quant Biol 2020;8(1):11–9.
[19] Khan H, Ibrahim M, Abdel-Aty AH, Khashan MM, Khan FA, Khan A. A fractional order Covid-19 epidemic model with Mittag-Leffler kernel. Chaos Solitons Fractals 2021;148:111030.
[20] Chretien JP, Riley S, George DB. Mathematical modeling of the West Africa Ebola epidemic. eLife 2015;4:e09186.
[21] Begum R, Tunç O, Khan H, Gulzar H, Khan A. A fractional order Zika virus model with Mittag–Leffler kernel. Chaos Solitons Fractals 2021;146:110898.
[22] Gaitán-Vélez V, Esquivel-Patino GG, Jiménez-Gutiérrez A. Environmental and economic analysis of a natural gas combined cycle power plant using CO2 utilization technologies and ecosystem services. ACS Sustain Chem Eng 2023;11(18):7218–30.
[23] Gallasch R, Efremova M, Charoentong P, Hackl H, Trajanoski Z. Mathematical models for translational and clinical oncology. J Clin Bioinform 2013;3:1–8.
[24] Salehi H, Vahidi J, Abdeljawad T, Khan A, Rad SY. A SAR image despeckling method based on an extended adaptive Wiener filter and extended guided filter. Remote Sens 2020;12(15):2371.
[25] Thirthar AA, Abboubakar H, Khan A, Abdeljawad T. Mathematical modeling of the COVID-19 epidemic with fear impact. AIMS Math 2023;8(3):6447–65.
[26] Bedi P, Khan A, Kumar A, Abdeljawad T. Computational study of fractional-order vector-borne diseases model. Fractals 2022;30(05):2240149.
[27] Haleem A, Javaid M, Khan IH. Current status and applications of Artificial Intelligence (AI) in medical field: an overview. Curr Med Res Pract 2019;9(6):231–7.

[28] Rong G, Mendez A, Assi EB, Zhao B, Sawan M. Artificial intelligence in healthcare: review and prediction case studies. Eng 2020;6(3):291–301.
[29] Sundar R, Gangopadhyay A, Gupta TR, Murthy PS, Gogula S, Sharath MN, et al. Heart health prediction and classification: an IoMT and AI collaborative model. In: MATEC web of conferences, vol. 392; 2024. p. 01142.
[30] Khan M, Shiwlani A, Qayyum MU, Sherani AM, Hussain HK. AI-powered healthcare revolution: an extensive examination of innovative methods in cancer treatment. BULLET: Jurnal Multidisiplin Ilmu 2024;3(1):87–98.
[31] Cui Z, Jing X, Zhao P, Zhang W, Chen J. A new subspace clustering strategy for AI-based data analysis in IoT system. IEEE Internet Things J 2021;8(16):12540–9. https://doi.org/10.1109/JIOT.2021.3073231.
[32] Fisher D, Lenz HJ, editors. Learning from data: artificial intelligence and statistics V. Springer Science & Business Media; 1996.
[33] Bhat SA, Huang NF. Big data and AI revolution in precision agriculture: survey and challenges. IEEE Access 2021;9:110209–22. https://doi.org/10.1109/ACCESS.2021.3102481.
[34] Ballabio D, Vasighi M. A MATLAB toolbox for Self Organizing Maps and supervised neural network learning strategies. Chemom Intell Lab Syst 2012;118:24–32. https://doi.org/10.1016/j.chemolab.2012.07.002.
[35] Atangana A. Fractal-fractional differentiation and integration: connecting fractal calculus and fractional calculus to predict complex system. Chaos Solitons Fractals 2017;102:396–406. https://doi.org/10.1016/j.chaos.2017.06.007.
[36] Atangana A, Akgül A, Owolabi KM. Analysis of fractal fractional differential equations. Alex Eng J 2020;59(3):1117–34. https://doi.org/10.1016/j.aej.2020.01.017.
[37] Partohaghighi M, Mortezaee M, Akgül A, Hassan AM, Sakar N. Numerical analysis of the fractal-fractional diffusion model of ignition in the combustion process. Alex Eng J 2024;86:1–8. https://doi.org/10.1016/j.aej.2024.05.002.
[38] Khan H, Rajpar AH, Alzabut J, Aslam M, Etemad S, Rezapour S. On a fractal–fractional-based modeling for influenza and its analytical results. Qual Theory Dyn Syst 2024;23(2):70. https://doi.org/10.1007/s12346-024-00314-0.
[39] Khan H, Alzabut J, Shah A, He ZY, Etemad S, Rezapour S, et al. On fractal-fractional waterborne disease model: a study on theoretical and numerical aspects of solutions via simulations. Fractals 2023;31(04):2340055. https://doi.org/10.1142/S0218348X23400554.
[40] Khan H, Alzabut J, Shah A, Etemad S, Rezapour S, Park C. A study on the fractal-fractional tobacco smoking model. AIMS Math 2022;7(8):13887–909. https://doi.org/10.3934/math.2022118.
[41] Earth.com. Global warming. Available at: https://www.earth.com/_next/image/?url=https. [Accessed 18 July 2024].
[42] Verma M, Verma AK. Effect of plantation of genetically modified trees on the control of atmospheric carbon dioxide: a modeling study. Nat Resour Model 2021;34(2):e12300. https://doi.org/10.1111/nrm.12300.
[43] https://www.shutterstock.com/image-photo/big-data-technology-science-scientist-querying-2255695571.

Dr. J. F. Gómez-Aguilar received the B.S. degree and M. Eng., in electrical engineering from Guanajuato University in 2005 and 2007, respectively, and Ph.D. degree in Physical from DCI, Guanajuato University in 2012. He is member of the Science and Technology National Council Engineering and Industry Recognized Referees Record (CONACYT-RCEA MEXICO). He is currently a full research professor at the Electronics Engineering Department of the National Research and Technological Development Center (CENIDET), Cuernavaca, Mor., Mexico. His scientific interests are fractional calculus, image and signal processing, control, electrochemistry, bioelectromagnetism and biomedical applications. He is serving as guest editor of some special issues, and also reviewer of more than 40 international accredited journals. He has presented and participated in more than 10 international conferences, also is author of more than 410 papers published in international journals with strict revision. His research interests are nonlinear dynamics, control theory, computational complexity, fractional dynamics, iterative methods, integral transforms and applications, signal processing, biomathematics, mathematical physics and variable order fractional calculus and applications.